CHALMERS
UNIVERSITY OF TECHNOLOGY

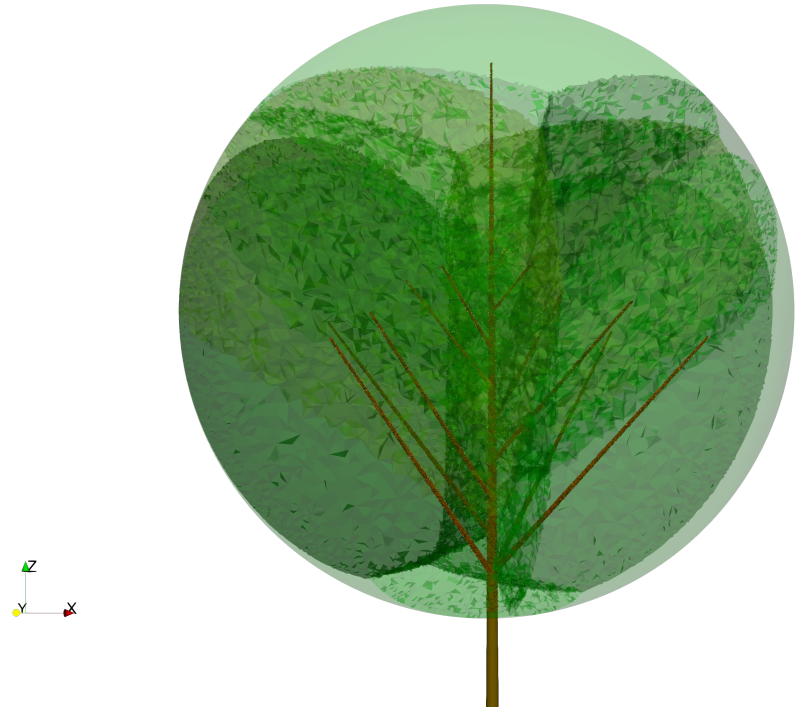

A Study on Single Tree Modeling for Wind-Induced Fluid–Structure Interaction

Exploring the Level of Detail for Tree Representation

Master's thesis in Applied Mechanics, MSc (MPAME)

John Paul Perumadan Mannummal

Department of Industrial and Materials Science
CHALMERS UNIVERSITY OF TECHNOLOGY
Gothenburg, Sweden 2025

Master's thesis in Applied Mechanics, MSc (MPAME)
2025

A Study on Single Tree Modeling for Wind-Induced Fluid–Structure Interaction

Exploring the Level of Detail for Tree Representation

John Paul Perumadan Mannummal

CHALMERS
UNIVERSITY OF TECHNOLOGY

Department of Industrial and Materials Science
Chalmers University of Technology
Gothenburg, Sweden 2025

A Study on Single Tree Modeling for Wind-Induced Fluid–Structure Interaction: Exploring the Level of Detail for Tree Representation
Master's thesis in Applied Mechanics, MSc (MPAME)
John Paul Perumadan Mannummal

Supervisor: Franziska Hunger, franziska.hunger@fcc.chalmers.se &
Gustav Kettil, gustav.kettil@fcc.chalmers.se
Examiner: Knut Andreas Meyer, knut.andreas.meyer@chalmers.se

Master's thesis in Applied Mechanics, MSc (MPAME) 2025
Department of Industrial and Materials Science
Chalmers University of Technology
SE-412 96 Gothenburg
Telephone +46 31 772 1000

Cover: A 12 branch partitioned tree crown model.

Typeset in LaTeX
Gothenburg, Sweden 2025

A Study on Single Tree Modeling for Wind-Induced Fluid–Structure Interaction: Exploring the Level of Detail for Tree Representation
Master's thesis in Applied Mechanics, MSc (MPAME)

John Paul Perumadan Mannummal

Department of Industrial and Materials Science
Chalmers University of Technology

Abstract

Trees and green spaces are vital for sustainable urban living, yet tools to guide optimal tree placement and assess wind related risks remain limited. This study presents a numerical modeling framework for simulating wind-induced fluid-structure interaction (FSI) on a single tree. Three tree models of increasing level of detail (LoD) are developed, and detailed FEM and CFD parameter studies are conducted to identify key mechanical and aerodynamic properties. Rather than relying on a detailed CAD model, the tree geometry is defined through spatial functions, allowing for the assignment of material and permeability properties to stem and crown regions within a single mesh used by both solvers. The immersed boundary method (IBM) is employed to capture tree motion in the CFD simulations. Through FEM parameter studies, a set of material properties for the artificial crown is proposed, identifying that a stiffness on the order of 10^2 Pa is necessary to observe wind-induced deformations. The study also evaluated how modeling the stem as a permeable object rather than a solid body affects the aerodynamic forces and wake properties. It was found that a permeable stem yields aerodynamic forces and velocity fields comparable to those of a solid stem. However for both types of stem, the aerodynamic influence of the stem is confined to its immediate vicinity. Beyond the crown's radial extent, the presence or absence of a stem showed negligible impact on the flow field. The results further highlight the dominant role of crown permeability in determining aerodynamic loading and wake characteristics, underscoring the importance of measurement-based permeability inputs for crown. Overall, the study demonstrates the feasibility and current limitations of the proposed modeling approach, providing a foundation for future FSI based tree–wind interaction studies.

Keywords: Tree Modeling, Tree-Crown Modeling, Fully Permeable Tree, Level of Detail, Wind-Tree Interaction, Fluid Structure Interaction, CFD, FEM

Acknowledgements

I would like to sincerely thank my supervisors and examiner for their immense and unwavering guidance throughout this project. Their commitment to quality and dedicated involvement made this a true team effort.

This thesis is part of the DUT project Urban ElemenTREE with financial support from the Swedish Research Council for Sustainable Development Formas under the grant 2024-01221. This work is also part of the Digital Twin Cities Centre supported by Sweden's Innovation Agency Vinnova under Grant No. 2024-03904.

John Paul Perumadan Mannummal
Gothenburg, August 2025

Acronyms

ABL Atmospheric Boundary Layer.

BT Branched Tree.

CFD Computational Fluid Dynamics.

DBH Diameter at Breast Height.

FCC Fraunhofer-Chalmers Centre.
FEM Finite Element Method.
FSI Fluid–Structure Interaction.

GS-FSI Gauss-Seidel FSI.

IB Immersed Boundary.
IBM Immersed Boundary Method.
IBOFlow Immersed Boundary Octree Flow Solver.

LAD Leaf Area Density.
LaStFEM FEM Structural Solver.
LoD Level of Detail.

MRE Mean Relative Error.

PAD Plant Area Density.
PAD-crown Plant Area Density of Crown Cell.
PAD-wood Plant Area Density of Wood Cell.
PT Partitioned Tree.

RANS Reynolds-Averaged Navier-Stokes.

ST Simple Tree.

TLS Terrestrial Laser Scanning.

VIVs Vortex Induced Vibrations.

Contents

Nomenclature

General

A_{PAD}	:	Plant area density (PAD) [m^2/m^3]
Stiffness_ratio	:	Ratio of Young's modulus of crown material to that of the stem material
Density_ratio	:	Ratio of density of crown material to that of the stem material

FEM Theory

E	:	Young's modulus [Pa]
ν	:	Poisson's ratio
$\boldsymbol{\sigma}$	:	Stress vector in Voigt notation [Pa]
$\boldsymbol{\epsilon}$	:	Strain vector in Voigt notation
$\tilde{\boldsymbol{\nabla}}$	:	Matrix differential operator [1/m]
$\boldsymbol{b}$	:	Body force vector [N/m^3]
$\boldsymbol{u}$	:	Exact local displacement vector [m]
$\delta\boldsymbol{u}$	:	Virtual displacement vector [m]
$\boldsymbol{x}$	:	Position vector [m]
$\boldsymbol{U}_i$	:	Nodal displacement at node i [m]
$\boldsymbol{U}$	:	Global nodal displacement vector [m]
$\delta\boldsymbol{u}_h$	:	Virtual displacement field (FEM approx.) [m]
$\delta\boldsymbol{U}$	:	Virtual nodal displacement vector [m]
$\boldsymbol{B}$	:	Strain-displacement matrix [1/m]
$\boldsymbol{D}$	:	Constitutive matrix [Pa]
$\boldsymbol{K}^e$	:	Element stiffness matrix [N/m]
$\boldsymbol{F}^e$	:	Element force vector [N]
$\boldsymbol{K}$	:	Global stiffness matrix [N/m]
$\boldsymbol{F}$	:	Global force vector [N]
C^0	:	Space of continuous functions
Ω	:	Domain
$\bar{\boldsymbol{t}}$	:	Traction vector [Pa]

Γ_t, Γ_u	:	Neumann / Dirichlet boundaries
n_{node}	:	Number of nodes per element
$N_i(\boldsymbol{x})$	:	Shape function for node i
$\boldsymbol{N}(\boldsymbol{x})$	:	Vector of shape functions
a_i, b_i, c_i, d_i	:	Coefficients of linear shape function N_i
Ω^e	:	Domain of element e
Γ_t^e	:	Neumann boundary of element e

CFD Theory

$\boldsymbol{u}$	:	Local velocity vector [m/s]
p	:	Local pressure [Pa]
ρ	:	Fluid density [kg/m^3]
ν	:	Kinematic viscosity [m^2/s]
ν_t	:	Turbulent (eddy) viscosity [m^2/s]
k	:	Turbulent kinetic energy [m^2/s^2]
ϵ	:	Turbulent dissipation rate [m^2/s^3]
σ_k	:	Turbulent Prandtl number for k transport
$c_{1\epsilon}, c_{2\epsilon}$	:	Model constants
C_μ	:	Eddy viscosity model constant
A_0, A_s	:	Model constants
Ω_{ij}	:	Rotation rate tensor [1/s]
S_u	:	Momentum source term [N/m^3]
S_ϵ	:	Turbulent dissipation source term [m^2/s^4]
C_d	:	Drag coefficient
β_p, β_d	:	Model coefficients
$C_{\epsilon 4}, C_{\epsilon 5}$	:	Model constants
z	:	Height above ground [m]
u^*_{ABL}	:	Friction velocity in atmospheric boundary layer [m/s]
κ	:	von Karman constant
H_{ref}	:	Reference height [m]
u_{ref}	:	Velocity at reference height [m/s]
z_0	:	Aerodynamic roughness length [m]

List of Figures

List of Tables

1
Introduction

According to data published by the United Nations (UN), the urban population is steadily increasing and is expected to exceed 50 percent of the global population by 2030 [23]. In response, urban expansion is also happening rapidly. In this context, ensuring the sustainability of urban living spaces is both critical and challenging.

The World Health Organization (WHO) recommended per-capita area of urban green space for the physical and mental well-being of a person is 9 m^2 [31]. With cities responsible for 70 percent of global CO_2 emissions [18], it is also critical to maintain sufficient vegetation to serve as a CO_2 sink. Inadequate vegetation and poor planning of urban green spaces can negatively impact the urban microclimate [35, 28].

Realizing the vital role of vegetation in sustainable urban development, efforts are required to restore lost green spaces, manage existing ones effectively, and find a balance between green and built spaces during urban expansion. The importance of urban trees in this endeavor cannot be overstated. However, urban trees face many limitations related to the scarcity of space, high costs, and the often-challenging conditions reducing the longevity of trees.

In Sweden, wind is a major factor influencing tree establishment, growth, and potential mechanical failure. However, our practical understanding of the interplay between wind and trees remains extremely limited. Consequently, there is limited information on optimal positioning when planting new trees. Further, our assessment of the risk for wind-induced tree failures, due to wind-throw (uprooting) or wind breakage (branch or trunk damage), often falls short. Therefore, urban decision makers, planners, and other stakeholders are in need of tools supporting evidence based urban greening strategies.

To investigate the vulnerability of existing trees to the expansion of built spaces and to support the planning of new tree placement, Computational Fluid Dynamics (CFD) simulations in conjunction with Finite Element Method (FEM) based tree models can be employed. Different approaches to modelling trees, with varying Level of Detail (LoD), exist in the literature. In the context of urban microclimate simulations the required LoD of individual trees has been a topic of discussion over the recent years [44, 10, 11, 47].

With expanding access to methods like Terrestrial Laser Scanning (TLS) which employs technologies like Light Detection and Ranging (LiDAR), the definition of LoD in individual trees are changing. An extensive review of existing definitions of LoD for trees is done by Xu et al. in their work [44]. According to Xu et al., a set of

tree parameters are used in defining the LoD for trees in the context of urban microclimate simulations. These include tree dimension, canopy geometry, Leaf Area Density (LAD) and leaf type.

In general, existing models for individual trees have primarily been employed to investigate airflow patterns around trees and their effects on the urban microclimate [13, 1, 8, 29, 9, 5], as well as to study the mechanical response of trees to wind loading [14, 45, 33, 2]. Among the works focused on the former category, the LoD varied from 2D to volumetric representations, with partial or no consideration of the tree skeleton. Most of these models used permeability-based approaches involving source term modifications to account for through-flow variations in tree crown. They typically relied on common assumptions such as constant aerodynamic and permeability properties like drag coefficient and LAD. In the latter category, the LoD ranged from simplified mechanical representations for FEM, such as cantilever beam models for the stem, to FEM models based on highly detailed tree skeletons reconstructed from TLS point cloud data.

However, as pointed out by Xu et al [44]., both excessive geometric detail and oversimplification that neglects key physical characteristics can render existing models impractical and inefficient for urban microclimate simulations. The literature review highlights the absence of a robust and computationally efficient tree representation model suitable for such applications.

From the literature review, it was also evident that, hardly any literature exists on modelling tree motion, considering a permeable crown. A recent work explore the bending of a simplified tree under simplified fluid conditions [2]. Yet, as trees adapt to the prevailing wind conditions, streamlining effects, crown reconfiguration and movement are important measures to reduce the force on the tree. Experiments of single tree measurements under different wind conditions have shown these effects [46, 22]. A numerical model that captures these effects enables further studies on forces exerted on trees in different urban environments, risk estimation of trees and might improve the prediction of the flow field downstream of the trees, being an important characteristic for urban planning.

1.1 Aim & Goals

Develop a parametric numerical model of a single tree that balances level of detail and physical accuracy, suitable for analyzing its structural and aerodynamic responses to wind using Fluid–Structure Interaction (FSI) simulations.

To achieve this, a FSI based modeling approach will be adopted for the proposed tree models. Emphasis is placed on streamlining the model generation pipeline to facilitate scalability of the study across different tree species and geometries.

The goal will be accomplished through several sub-objectives that guide the development and integration of both structural and fluid dynamic components.

- Modelling of the tree as a single unified mesh, thereby eliminating the need for spatial coupling between the stem and crown in the FEM and CFD solvers.
- Developing an FEM model capable of capturing the key dynamics of both the tree skeleton and the tree crown.
- Conducting a FEM parameter study to identify and quantify the artificial material properties most relevant to accurately modeling the tree crown.
- Developing a CFD model capable of capturing variation of flow properties over and through the tree-crown.
- Conducting a CFD parameter study to identify appropriate permeability properties for the permeable stem and crown within the single-object tree representation.
- Analysis of the developed tree models using physical reasoning of structural and aerodynamic responses in FSI simulations.

The LoD for the proposed tree representations includes the following aspects:

- **Dimension:** True-to-scale tree geometry.
- **Tree skeleton:** A tapered cylindrical cantilever stem with tapered cylindrical first-order branches.
- **Tree crown:** Represented as a spherical volume with internal partitions; through-flow is modeled using source-term modification permeability models.
- **Plant Area Density (PAD):** Defined as spatial fields within the crown volume.

1.2 Limitations

The following aspects which are relevant in an actual tree are neglected or approximated in this study:

- Soil mechanics and related root-plate effects of the tree are neglected.
- Instead of fully resolving the flow through the tree crown, permeability models are used to model variation of through flow properties.
- The specific modelling approach approximates the solid behavior of stem using a fluid object with very low permeability.

Further in the report, Chapter 2 discusses the relevant supporting theory for the structural and fluid dynamics concepts used in the development of the tree models. Chapter 3 details the development process, covering the FEM and CFD components of the framework. In Chapter 4, the results and discussion of the FSI simulations conducted using the developed tree models are presented. The report concludes with a discussion of the overall framework, key insights obtained, and suggestions for future work in Chapter 5.

2

Theory

2.1 Wind-Tree Interaction

In this section, a basic introduction to the bio-mechanical description of a tree, definition of PAD, different scales present in tree motion and relevant peculiarities of forest grown Aspen tree that led to the choice of it for the study are given.

2.1.1 Tree Nomenclature

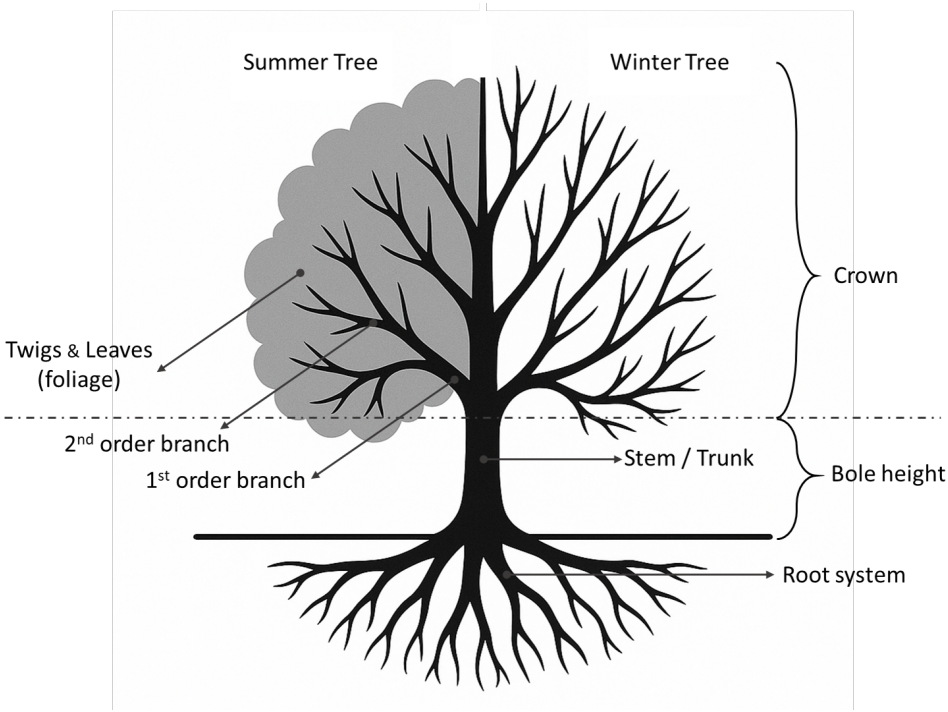

Figure 2.1: Tree nomenclature used in the study.

Structurally, the root system anchors the tree and makes it stable under wind and other external loading. Structure of the tree extends from the root system into the stem and then into first order and higher order branches. Depending on the nature of external stimuli like wind direction, exposure to sunlight and presence of obstacles, the morphology of the tree structure will vary in order to adapt to such stimuli. Open grown trees are subjected to relatively higher wind loads, and this causes such trees to have thicker stem than forest grown trees which tend to have

long and narrow stem. Also features like buttressing at the roots are predominant in open grown trees. Similar morphological evolution of trees is collectively termed thigmomorphogenesis [6].

Bole height is measured along the main-stem from the ground to the starting point (node) of the first branch. The crown comprises of the leaves, twigs and higher order branches above the bole height. The collective mass of leaves and twigs are often called foliage. The largest branches are called first order branches. And the branches that grows laterally from the first order branches are termed second order and so on. A discussion of the growth characteristics of a tree is presented by Franklin. J and Mercker. D in their work [16]. A pictorial representation of tree nomenclature is given in Figure 2.1.

2.1.2 Plant Area Density

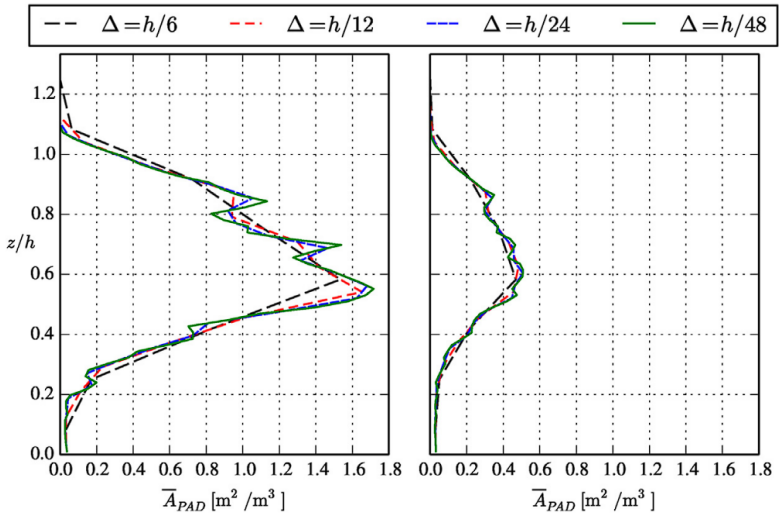

Figure 2.2: PAD distribution with leaves (left) and without leaves (right) estimated for single tree using TLS and varying grid resolution, taken from [8].

Plant Area Density (PAD) is defined as the sum of one-sided plant surface area (windward facing area) in unit volume. PAD has the units $m^2 \cdot m^{-3}$. In contrast to LAD in which only one-sided leaf area is considered, the PAD includes one-sided area of all material parts including leaves, branches and the stem. Measurements of PAD can be made using TLS method. A detailed study measuring PAD of single tree using TLS is done by Dellwik et al. in their work [8]. The measured PAD distributions for a single tree, taken from their work is given in Figure 2.2 for reference.

2.1.3 Scales of Motion in Trees

The wind induced dynamic response of a tree occurs at different scales. This multi-scale response helps the trees to dissipate the kinetic energy transferred by the wind via aerodynamic loads. These scales of motion include:

- Large scale bending and sway motion of the entire tree.
- Intermediate scale buffeting motion of branches.
- Small scale fluttering motion of leaves.

In general, these motions get initiated when the aerodynamic force disturbs the static equilibrium position of the tree corresponding to no-wind condition. For steady wind conditions, the tree will try to re-adjust itself to a modified equilibrium position. With fluctuating wind flow, these motions can persist longer with different amplitudes. With complex architecture of a tree, higher number of modes and degrees of freedom can exist in the tree [15], making it often difficult to find an equilibrium state even in low wind conditions. Also, high wind conditions can result in high amplitude oscillations of branches or the entire tree by self excitation or resonance by Vortex Induced Vibrations (VIVs) [36].

Such motions can lead to structural failures like stem breakage or uprooting as well as create airflow patterns downstream. While the sway motions add to the canopy scale eddies, the buffeting of branches and motion of the leaves (collectively called foliage motion) create small scale eddies in the flow field. Within the foliage motion, the individual leaf motion predominates over effects due to motion of branches. Foliage motion makes the aerodynamic characteristics of the crown like drag coefficient and PAD, a function of time. This change of properties induced by foliage motion is termed reconfiguration of the crown. A clear discussion of the foliage dynamics and its effects on the wind is discussed in detail by Tadrist et al. in their work [36].

2.1.4 European Aspen Tree (Populus tremuloides)

Figure 2.3: Open grown Swedish columnar Aspen (left) and forest grown (right) American Aspen tree [38].

Aspen (Populus tremuloides) is a large, fast-growing broad-leaf tree. They are characterized by a very narrow growing stem. Based on the growing conditions, PAD distributions of trees will vary. Forest grown Aspen trees seems to have a slender form with small spherical crown at the top of the narrow stem, while open grown

trees like those in urban setting usually have short stem and cylindrical crown shapes. Reference images showing the overall geometry of the columnar Swedish Aspen and a forest grown American Aspen tree are shown in Figure 2.3. Its unique ability of regrowth into multiple new trees from its own root system makes it attractive to the wood industry. A detailed discussion about the role of Aspen trees in serving bio-diversity, carbon sequestration, wood industry and other commercial needs is presented by Rogers et al. in their review article [30]. The choice of forest grown Aspen trees for the study is primarily due to its simplicity in structure and overall form.

2.2 Finite Element Method

This section outlines the fundamental concepts relevant to the FEM simulations conducted in the study. A brief overview of the small-strain linear elasticity model which was used to describe the material behavior of the tree elements is provided. Further, the weak formulation leading to finite element discretization of the governing equations for a linear elastic solid and a mathematical description of static equilibrium analysis in FEM are also presented.

Supporting theory for FEM discussed in this report are based on concepts explained in the book *Introduction to the Finite Element Method* [24].

2.2.1 Small Strain Elasticity

When strains and rotations are small, and for materials that exhibit no strain-softening, a small-strain theory based on kinematics, equations of motion, and constitutive laws is commonly used. The basic assumptions of purely mechanical behavior, reversibility, and path-independence imply the absence of energy dissipation during deformation. The energy expended in deforming the material is stored as strain energy, which is fully recoverable upon unloading.

The regime of linear elastic behavior is typically confined to small strain magnitudes, which is why the small-strain elasticity theory is used to model such materials.

For a linear elastic material, stress is related to strain via the constitutive relation known as Hooke's law. For a general three-dimensional isotropic elastic material, this relation can be written in matrix (Voigt) notation as:

$$\boldsymbol{\sigma} = \mathbf{D}\,\boldsymbol{\epsilon} \tag{2.1}$$

$$\mathbf{D} = \frac{E}{(1+\nu)(1-2\nu)} \begin{bmatrix} 1-\nu & \nu & \nu & 0 & 0 & 0 \\ \nu & 1-\nu & \nu & 0 & 0 & 0 \\ \nu & \nu & 1-\nu & 0 & 0 & 0 \\ 0 & 0 & 0 & \frac{1-2\nu}{2} & 0 & 0 \\ 0 & 0 & 0 & 0 & \frac{1-2\nu}{2} & 0 \\ 0 & 0 & 0 & 0 & 0 & \frac{1-2\nu}{2} \end{bmatrix}$$

Here, $\boldsymbol{\sigma}$ is the 6-component stress vector, $\boldsymbol{\epsilon}$ is the 6-component strain vector, and $\mathbf{D}$ is the constitutive matrix containing the elastic moduli. E is the Young's modulus and ν is the Poisson's ratio.

2.2.2 Governing Equations in Structural Mechanics

In the context of small-strain linear elasticity, the governing equations in their strong form consist of the equilibrium equation (or conservation of linear momentum), the constitutive relation linking internal stresses to strains, and the kinematic relation expressing strain in terms of displacement. These equations form the foundation of the finite element formulation and are given as follows:

1. **Equilibrium Equation (Cauchy Momentum Balance)**

$$\tilde{\nabla}^T \boldsymbol{\sigma} + \mathbf{b} = \mathbf{0} \tag{2.2}$$

   where $\mathbf{b}$ is the body force vector per unit volume. $\tilde{\nabla}$ is the matrix differential operator.

2. **Constitutive Equation (Hooke's Law)**:

$$\boldsymbol{\sigma} = \mathbf{D}\boldsymbol{\epsilon} \tag{2.3}$$

3. **Kinematic Equation (Strain-Displacement Relation)**:

$$\boldsymbol{\varepsilon} = \tilde{\nabla}\mathbf{u} \tag{2.4}$$

   where $\mathbf{u}$ is the displacement vector.

Governing equations 2.2, 2.3 and 2.4 together with the respective Dirichlet and Neumann boundary conditions, constitute the strong formulation (i.e., the original set of differential equations) of the linear elasticity problem. The strong formulation must be satisfied point-wise throughout the entire domain and therefore defines the exact state of the system.

2.2.3 Weak Formulation

While the strong form requires the solution to satisfy the differential equations point-wise and demands higher order continuity and differentiability, this is often too restrictive for complex geometries and discontinuous material properties.

To overcome these limitations, we introduce the weak form, which is based on a variational principle. In the context of linear elasticity, this variational principle corresponds to the principle of virtual work. According to this principle, the total virtual work done by internal stresses is equal to the total virtual work done by external forces for all kinematically admissible virtual displacements.

Instead of enforcing the equilibrium equation point-wise, the weak form ensures that the equation is satisfied in an integral sense over the domain. This approach allows us to relax the differentiability requirements of the trial solution.

By integrating the equilibrium equation against a set of suitably chosen test functions (typically piecewise continuous functions from a C^0 function space, such as linear Lagrange polynomials), the requirement for the displacement field to be twice differentiable is reduced to only once differentiable. This makes the method well-suited for piecewise polynomial approximations commonly used in the finite element method.

Furthermore, by applying the Gauss divergence theorem, the spatial derivatives acting on the stress field are transferred to the test functions. This avoids the need to directly differentiate the stress components, which is particularly beneficial when stresses are derived from displacements via constitutive laws.

The weak form, derived using the principle of virtual work, is obtained from the strong form equation (2.2) as follows:

We begin by multiplying the equilibrium equation by a virtual displacement $\delta \boldsymbol{u} \in \mathcal{V}$ (test function space), such that $\delta \boldsymbol{u} = \boldsymbol{0}$ on the Dirichlet boundary Γ_u (where actual displacements are prescribed). We then integrate the resulting expression over the domain Ω:

$$\int_\Omega \delta \boldsymbol{u}^T (\nabla \cdot \boldsymbol{\sigma}) \, d\Omega + \int_\Omega \delta \boldsymbol{u}^T \boldsymbol{b} \, d\Omega = 0 \tag{2.5}$$

Applying the divergence theorem (i.e., integration by parts) to the first term allows the derivative to be transferred from the stress tensor $\boldsymbol{\sigma}$ to the virtual displacement $\delta \boldsymbol{u}$, reducing the differentiability requirements on the solution. This yields::

$$-\int_\Omega \boldsymbol{\varepsilon}(\delta \boldsymbol{u})^T \boldsymbol{\sigma} \, d\Omega + \int_\Gamma \delta \boldsymbol{u}^T (\boldsymbol{\sigma} \cdot \boldsymbol{n}) \, d\Gamma + \int_\Omega \delta \boldsymbol{u}^T \boldsymbol{b} \, d\Omega = 0 \tag{2.6}$$

Using the traction boundary condition $\boldsymbol{\sigma} \cdot \boldsymbol{n} = \bar{\boldsymbol{t}}$ on the Neumann boundary Γ_t, and noting that virtual displacement $\delta \boldsymbol{u} = 0$ on the Dirichlet boundary Γ_u, the boundary integral reduces to:

$$-\int_\Omega \boldsymbol{\varepsilon}(\delta \boldsymbol{u})^T \boldsymbol{\sigma} \, d\Omega + \int_{\Gamma_t} \delta \boldsymbol{u}^T \bar{\boldsymbol{t}} \, d\Gamma + \int_\Omega \delta \boldsymbol{u}^T \boldsymbol{b} \, d\Omega = 0 \tag{2.7}$$

Substituting the constitutive relation $\boldsymbol{\sigma} = \boldsymbol{D}\boldsymbol{\varepsilon}(\boldsymbol{u})$ into the expression yields the weak form of the linear elasticity problem:

$$\int_\Omega \boldsymbol{\varepsilon}(\delta \boldsymbol{u})^T \boldsymbol{D} \boldsymbol{\varepsilon}(\boldsymbol{u}) \, d\Omega = \int_\Omega \delta \boldsymbol{u}^T \boldsymbol{b} \, d\Omega + \int_{\Gamma_t} \delta \boldsymbol{u}^T \bar{\boldsymbol{t}} \, d\Gamma \tag{2.8}$$

Rearranging the weak form reveals that it corresponds to the first variation of the total potential energy functional, which must vanish for equilibrium. Thus, the weak form can also be interpreted as the variational statement of the principle of minimum potential energy, which holds for linear elastic materials.

2.2.4 Finite Element Discretization and Equilibrium Solver

To solve the weak form numerically using the finite element method, the unknown continuous displacement field $\boldsymbol{u}$ is approximated using a finite-dimensional basis function defined over the discretized domain. In this study, the domain is discretized

using four-node linear tetrahedral elements. Within each element, the displacement field is interpolated using piecewise linear shape functions associated with the element's nodes.

Accordingly, the displacement field $\boldsymbol{u}$ and virtual displacement $\delta\boldsymbol{u}$ are approximated as:

$$\boldsymbol{u}_h(\boldsymbol{x}) = \sum_{i=1}^{n_{node}} N_i(\boldsymbol{x})\boldsymbol{U}_i = \boldsymbol{N}(\boldsymbol{x})\boldsymbol{U} \tag{2.9}$$

$$\delta\boldsymbol{u}_h(\boldsymbol{x}) = \sum_{i=1}^{n_{node}} N_i(\boldsymbol{x})\delta\boldsymbol{U}_i = \boldsymbol{N}(\boldsymbol{x})\delta\boldsymbol{U} \tag{2.10}$$

where $\boldsymbol{U}$ are the nodal displacement vectors, and $\boldsymbol{N}(\boldsymbol{x})$ is the vector of shape functions.

For a linear tetrahedral element, the gradient of N_i is constant over the element and each N_i has the form:

$$N_i(x, y, z) = a_i + b_i x + c_i y + d_i z$$

The strain-displacement matrix $\boldsymbol{B}$ relates nodal displacements to strains via:

$$\boldsymbol{\varepsilon}(\boldsymbol{u}_h) = \boldsymbol{B}\boldsymbol{U}, \quad \boldsymbol{\varepsilon}(\delta\boldsymbol{u}_h) = \boldsymbol{B}\delta\boldsymbol{U}$$

Substituting these finite-dimensional approximations into the weak form results in a matrix expression at the element level:

$$\delta\boldsymbol{U}^T \left(\int_{\Omega^e} \boldsymbol{B}^T \boldsymbol{D}\boldsymbol{B}\, d\Omega \right) \boldsymbol{U} = \delta\boldsymbol{U}^T \left(\int_{\Omega^e} \boldsymbol{N}^T \boldsymbol{b}\, d\Omega + \int_{\Gamma_t^e} \boldsymbol{N}^T \bar{\boldsymbol{t}}\, d\Gamma \right) \tag{2.11}$$

From the above equation, the element stiffness matrix and element force vector are defined as:

$$\boldsymbol{K}^e = \int_{\Omega^e} \boldsymbol{B}^T \boldsymbol{D}\boldsymbol{B}\, d\Omega \quad \text{(element stiffness matrix)} \tag{2.12}$$

$$\boldsymbol{F}^e = \int_{\Omega^e} \boldsymbol{N}^T \boldsymbol{b}\, d\Omega + \int_{\Gamma_t^e} \boldsymbol{N}^T \bar{\boldsymbol{t}}\, d\Gamma \quad \text{(element force vector)} \tag{2.13}$$

To form the global system, all element matrices and vectors are assembled based on the global numbering of nodes and degrees of freedom:

$$\boldsymbol{K}\boldsymbol{U} = \boldsymbol{F} \tag{2.14}$$

where:

- $\boldsymbol{K} = \sum_e \boldsymbol{K}^e$ is the global stiffness matrix,
- $\boldsymbol{U}$ is the global displacement vector (unknowns),
- $\boldsymbol{F} = \sum_e \boldsymbol{F}^e$ is the global force vector.

For static and linear elasticity problems, the resulting sparse system is solved implicitly without time stepping, using a direct or iterative linear solver. Solving this system provides the displacement field that satisfies mechanical equilibrium under the given loading and boundary conditions.

2.3 Computational Fluid Dynamics

This section provides an overview of the methods and models used in CFD simulations from the study. The Immersed Boundary Method (IBM), as implemented in the Immersed Boundary Octree Flow Solver (IBOFlow) solver developed at Fraunhofer-Chalmers Centre (FCC) [19], is first introduced to describe how geometries are handled without the need for conformal meshing. Then, the governing equations solved by the steady Reynolds-Averaged Navier-Stokes (RANS) solver are presented along with the associated turbulence model. The permeability model used to represent the variation of flow properties within the tree crown is also discussed. Finally, the characteristics of the atmospheric boundary layer flow are outlined, as they are used to define the inlet boundary conditions for the CFD simulations in the study.

2.3.1 Immersed Boundary Method

Immersed boundary method uses a fixed cartesian grid. The boundary (surface mesh) of the object to be analyzed is inserted into this cartesian grid and thus the need for a rigorous body-fitted fluid mesh is avoided. Mesh refinement can be easily applied to the surrounding cartesian grid to accurately capture the geometry and flow features near the immersed object. In applications involving motion of objects in a fluid domain and in situations where large displacements in fluid domain is plausible, IBM can be computationally efficient and affordable compared to a adaptive meshing approach.

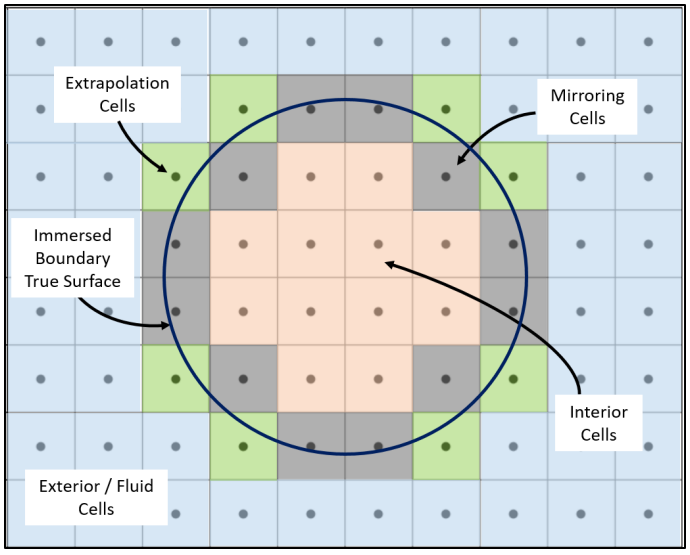

Figure 2.4: Cartesian grid with immersed boundary showing different cell types.

Once the boundaries are immersed into the cartesian grid, appropriate boundary conditions using forcing functions or source terms are incorporated into the cells lying in the vicinity of the boundary. Different Immersed Boundary (IB) methods exists in literature [27, 39]. In the IBOFlow solver used in the study, a mirroring

IB method [19] is used in which, the velocity is implicitly mirrored across the IB. To impose the no-slip boundary condition at the IB, the velocity at the mirroring cell is set such that a linear interpolation between the mirroring cell and the known velocity at the mirrored point yields exactly the local velocity of the IB. The fictitious velocities inside the solid are excluded from the continuity equation to ensure that no mass flux occurs across the IB.

The different cell types used to define cells in IB method is shown in Figure 2.4.

2.3.2 Governing Equations in Fluid Dynamics

For the study, a steady-state RANS CFD solver is used. Incompressible unsteady formulations of governing equations according to the model are discussed below [40]. RANS equations are solved in a segregated manner, with pressure velocity coupling using SIMPLEC method.

1. **The continuity equation**
   continuity equation or mass balance equation can be written in vector notation as:

$$\nabla \vec{u} = 0 \tag{2.15}$$

   Where $\vec{u}$ is the local velocity vector.
2. **The momentum equation**
   The momentum equation also called as Navier Stokes equation or momentum balance equation can be written in vector form as:

$$\frac{\partial \vec{u}}{\partial t} + \vec{u} \cdot \nabla \vec{u} = -\frac{\nabla p}{\rho} + \nabla \cdot \left((\nu + \nu_t) \nabla \vec{u} \right) \tag{2.16}$$

   where p is the local pressure, ρ is the fluid density, ν and ν_t are kinematic viscosity and turbulent viscosity respectively.

2.3.2.1 k-ϵ Realizable Turbulence Model

To solve for mean flow and turbulence, RANS equations are solved in conjunction with the k-ϵ Realizable eddy viscosity turbulence model. The closure problem arising in RANS equations is addressed using the Boussinesq approximation and solving for the transport of turbulent kinetic energy and turbulent dissipation rate.

The local turbulent kinetic energy is found by solving the transport equation for turbulent kinetic energy or the k-equation. And the realizable k-equation is given as:

3. **The k-equation**

$$\frac{\partial k}{\partial t} + \vec{u} \cdot \nabla k = \nabla \cdot \left((\nu + \frac{\nu_t}{\sigma_k}) \nabla k \right) + \nu_t S^2 - \epsilon \tag{2.17}$$

where $S = \sqrt{2 S_{ij} S_{ij}}$, S_{ij} is the strain rate tensor quantifying deformation of fluid volume, ϵ is the turbulent dissipation rate and σ_k is the turbulent Prandtl number.

The local turbulent dissipation rate is found by solving the transport equation for ϵ and is given as:

4. **The ϵ equation**

$$\frac{\partial \epsilon}{\partial t} + \vec{u} \cdot \nabla \epsilon = \nabla \cdot \left((\nu + \frac{\nu_t}{\sigma_k}) \nabla \epsilon \right) + c_{1\epsilon} S - C_{2\epsilon} \frac{\epsilon^2}{k + \sqrt{\nu \epsilon}} \tag{2.18}$$

$$\nu_t = C_\mu \frac{k^2}{\epsilon} \tag{2.19}$$

$$C_\mu = \frac{1}{A_0 + A_s \frac{kU^*}{\epsilon}} \tag{2.20}$$

where k is the local turbulent kinetic energy, $\eta = S\frac{k}{\epsilon}$,$c_{1\epsilon} = \max\left(0.43, \frac{\eta}{\eta+5}\right)$, $c_{1\epsilon} = 1.92$, $U^* = \sqrt{S_{ij}S_{ij} + \Omega_{ij}\Omega_{ij}}$, $A_0 = 4.04$, $A_s = \sqrt{6}\cos\phi$,$W = \frac{S_{ij}S_{jk}S_{ki}}{\sqrt{(S_{ij}S_{ij})^3}}$, $\phi = \frac{1}{3}\arccos(\sqrt{6}W)$.

2.3.3 Source Terms from Permeability Model Used in Study

To approximate the variation in flow properties inside the tree crown, permeability model with source terms found in literature [10] are used.

$$S_{\vec{u}} = -\rho C_d A_{PAD} \vec{u} |\vec{u}| \tag{2.21}$$

$$S_\epsilon = \rho C_d A_{PAD} \frac{\epsilon}{k} \left(C_{\epsilon 4} \beta_p |\vec{u}|^3 - C_{\epsilon 5} \beta_d |\vec{u}| k \right) \tag{2.22}$$

where:

ρ	:	density of fluid
C_d	:	drag coefficient
A_{PAD}	:	plant area density
β_p	:	fraction of mean kinetic energy converted into turbulent kinetic energy
$\vec{u}$	:	local velocity vector
β_d	:	dimensionless coefficient for short circuiting of turbulent cascade
k	:	local turbulent kinetic energy
ϵ	:	local dissipation rate
$C_{\epsilon 4}, C_{\epsilon 5}$	:	modal constants

The coefficients $\beta_p, \beta_d, C_{\epsilon 4}$ and $C_{\epsilon 5}$ used in the study are 1,1,0 and -2.556 respectively based on study by Dellwik et al.[8].

The above source terms are solved as additional terms in momentum, turbulent dissipation rate transport equations, at the internal cells of IB object.

Since the momentum and turbulent source terms are all functions of PAD, by setting a zero PAD value in a region, the permeability model can be switched off in those cells.

2.3.4 Atmospheric Boundary Layer Flow

The lower part of Atmospheric Boundary Layer (ABL) extending from the ground to an elevation of 200 m is characterized to be significant for studying different phenomena in urban microclimate, pollutant dispersion and deposition by wind and many more. In order to approximate the ABL flow, wall functions for velocity and turbulent flow properties are used in CFD. These wall functions are derived based on a number of assumptions like:

- Horizontal homogeneity and absence of streamwise gradients.
- Equilibrium between mean flow and turbulent properties with turbulence induced by ground roughness.
- Local equilibrium exists between turbulent production and dissipation.

Based on the above assumptions, following wall functions for fully developed ABL profiles of velocity, turbulent kinetic energy and turbulent dissipation rate are used [4]:

$$U(z) = \frac{u^*_{ABL}}{\kappa} ln(\frac{z + z_0}{z_0}) \tag{2.23}$$

$$k(z) = \frac{u^{*2}_{ABL}}{\sqrt{C_\mu}} \tag{2.24}$$

$$\epsilon(z) = \frac{u^{*3}_{ABL}}{\kappa(z + z_0)} \tag{2.25}$$

where:

u^*_{ABL}	:	ABL friction velocity
κ	:	von Karman constant (0.40–0.42)
C_μ	:	turbulent viscosity coefficient from standard k-ϵ turbulence model (0.09)
z	:	height measured from ground
z_0	:	aerodynamic roughness length

2.4 Fluid Structure Interaction

This section introduces the staggered FSI approach adopted in the study. The distinction between weak and strong coupling strategies is briefly discussed to clarify the level of interaction between the fluid and structural solvers. Finally, the Gauss-Seidel FSI (GS-FSI) solver used for the two-way coupled simulations is outlined.

2.4.1 FSI Coupling Algorithms

2.4.1.1 Monolithic & Staggered Approach

In the monolithic approach, the governing equations from fluid and solid domains are solved as a combined system of equations. While in a staggered (partitioned) approach, separate solvers for fluid and solid variables are used. Here, the interaction between physics is ensured by the use of a coupling algorithm between solvers. The

fundamental advantage of the staggered approach lies in the ability to use optimized solvers for the respective physics.

2.4.1.2 Strong (semi-monolithic) & Weak (explicit) Coupling

The coupling between physics is said to be strong if the case demands synchronization of all the system variables during every time-step [41, 43]. Cases involving large deformations and small time scales, in which both domains influence each other are examples of strong coupling. In applications where time scale of deformation is large or the feedback to flow is insignificant, weak or loosely coupled approach can be used. In weak coupling, both solvers progress one time-step in each iteration and no synchronization of variables between solvers are made. Based on the nature of the coupling, the choice of coupling scheme is made.

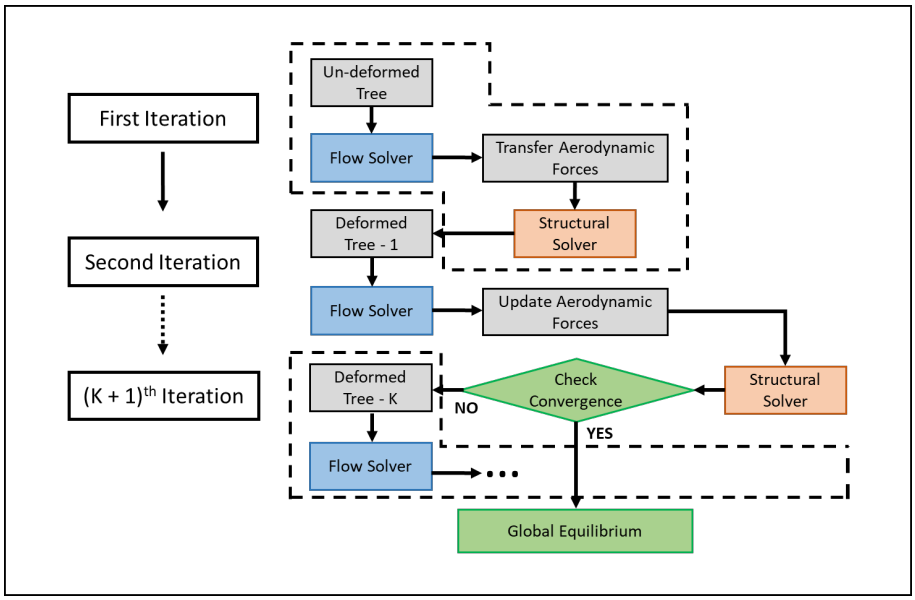

Figure 2.5: Working of a loosely coupled partitioned Gauss-Seidel FSI solver.

2.4.2 Gauss-Seidel FSI Solver

In this study, a GS-FSI solver is used to couple the structural and flow solvers. The basic working of the GS-FSI solver in a general two way coupled simulation is described in the Figure 2.5. The solver works in a sequential manner transferring aerodynamic forces and deformed tree geometry in each FSI iteration. Internal iterations are also included within each FSI iteration to ensure synchronization of variables between CFD and FEM and strong coupling [41]. During each FSI iteration, equilibrium of structural and flow properties is monitored using convergence of respective residuals. Once these residuals are within allowed tolerances for each solver, iterations are stopped.

In the case of one-way coupling, the feedback from structural solver to the flow solver is absent. During the first iteration, flow solver calculates the steady state flow field and forces on the tree using the undeformed tree geometry. Using the

solved pressure field, the structural solver solves for the static equilibrium geometry of the tree.

3
Methodology

As discussed in the beginning of the report, the objective of the study is to develop a single tree model suitable for investigating wind-tree interaction using FSI simulations. The proposed tree models and the FSI algorithm should avoid detailed modeling of tree morphology but instead at the same time be able to resolve the wind-tree interaction physics with sufficient realism. To achieve this, three tree geometries of increasing level of detail are used to study different modelling aspects of the tree-model. Using the basic tree geometry, the relevant material and aerodynamic parameters of the model are first established. These parameters are then progressively fine tuned for geometries with increased complexity.

In general, three main aspects are considered in the investigated tree models. These are:

1. Overall form of the tree - influencing its external aerodynamics.
2. Branching architecture (tree-skeleton) - which defines the mass, stiffness and damping characteristics of tree motion dynamics.
3. Variation of through flow properties in the tree crown - which affect the wake field dynamics.

The motivation and steps taken to choose different parameters of the tree-models, according to the above considerations and the planned objective are elaborated in the following sections.

3.1 Tree Representation Geometries

The three tree geometries are named as Simple Tree (ST), Branched Tree (BT) and Partitioned Tree (PT) respectively. In contrast to tree models having a solid stem-object and fluid crown-object, the proposed tree-models in common were defined as a single-object in the structural-solver and flow-solver. This approach ensures ease of implementation of the moving tree in the coupled FSI setup by eliminating the need for spatial coupling between stem and crown.

The discussed tree geometries are described in the following subsections starting with the ST. A graphical representation of the geometries are shown in Figure 3.1. Throughout the discussion, a right-handed cartesian coordinate system is followed with the tree at the origin, tree height along the positive Z axis and wind being uni-directional along the positive X axis.

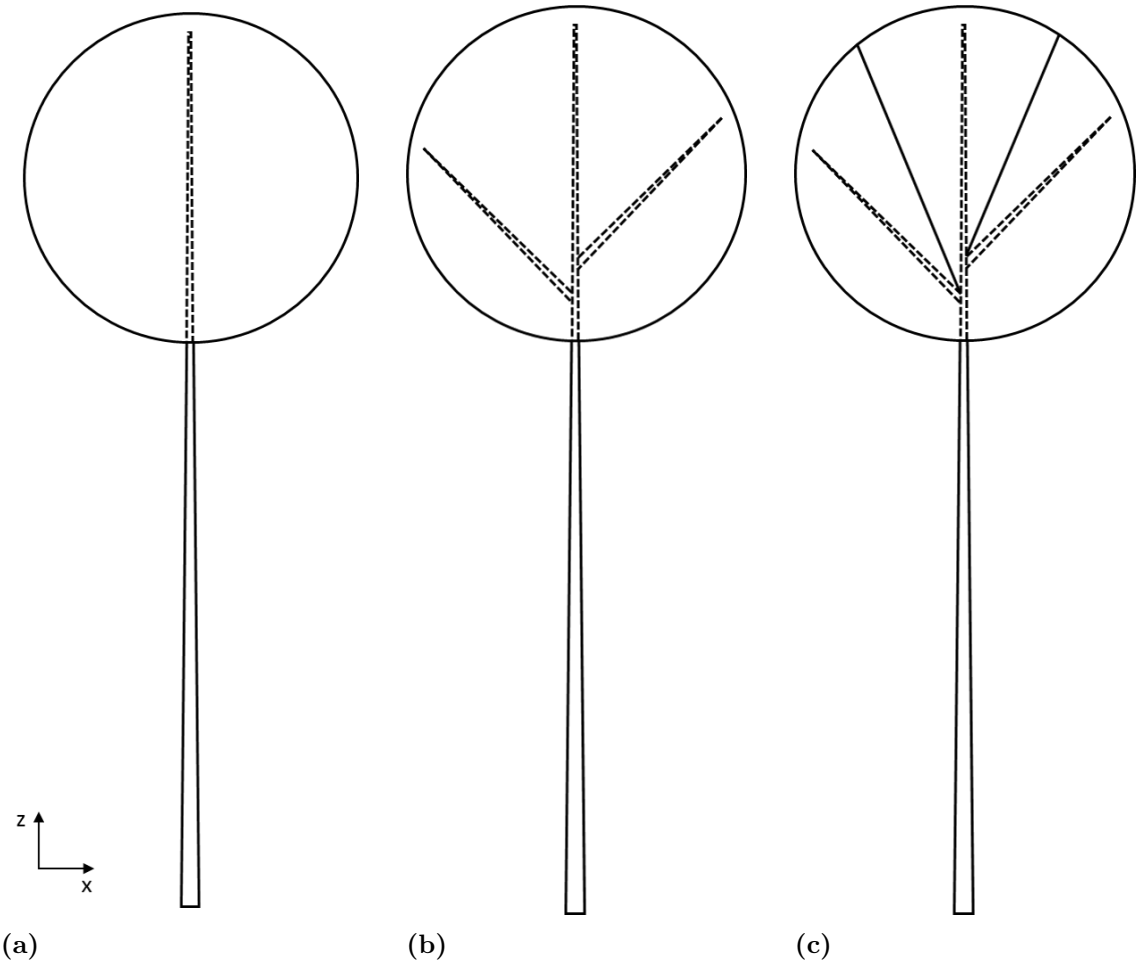

Figure 3.1: Tree representations. (a) Simple tree ; (b) Branched tree ; (c) Partitioned tree.

3.1.1 Simple Tree

The overall form of the ST corresponded with the real-scale reference forest grown Aspen tree. It is defined using a tapered cylindrical cantilever stem with a continuous spherical crown. The ST is set to resolve the external aerodynamics of the tree as well as the primary bending mode under aerodynamic load. The material properties of the cantilever stem are taken as the properties of European Aspen wood from the reference article [12].

Within the ST geometry, the stem extends from root defined with a root diameter, to the tip of the crown with a defined stem taper rate. The minimum cross-section diameter of the stem is constrained at the tip using a limiter. Further the crown radius and crown-center position are set to match the overall tree form. The diameter variation of the stem for the chosen taper rate is plotted in Figure 3.3. The magnitude of taper rate used in the study is also given in the Figure 3.3. The Diameter at Breast Height (DBH) for the stem is measured as 37.825 cm.

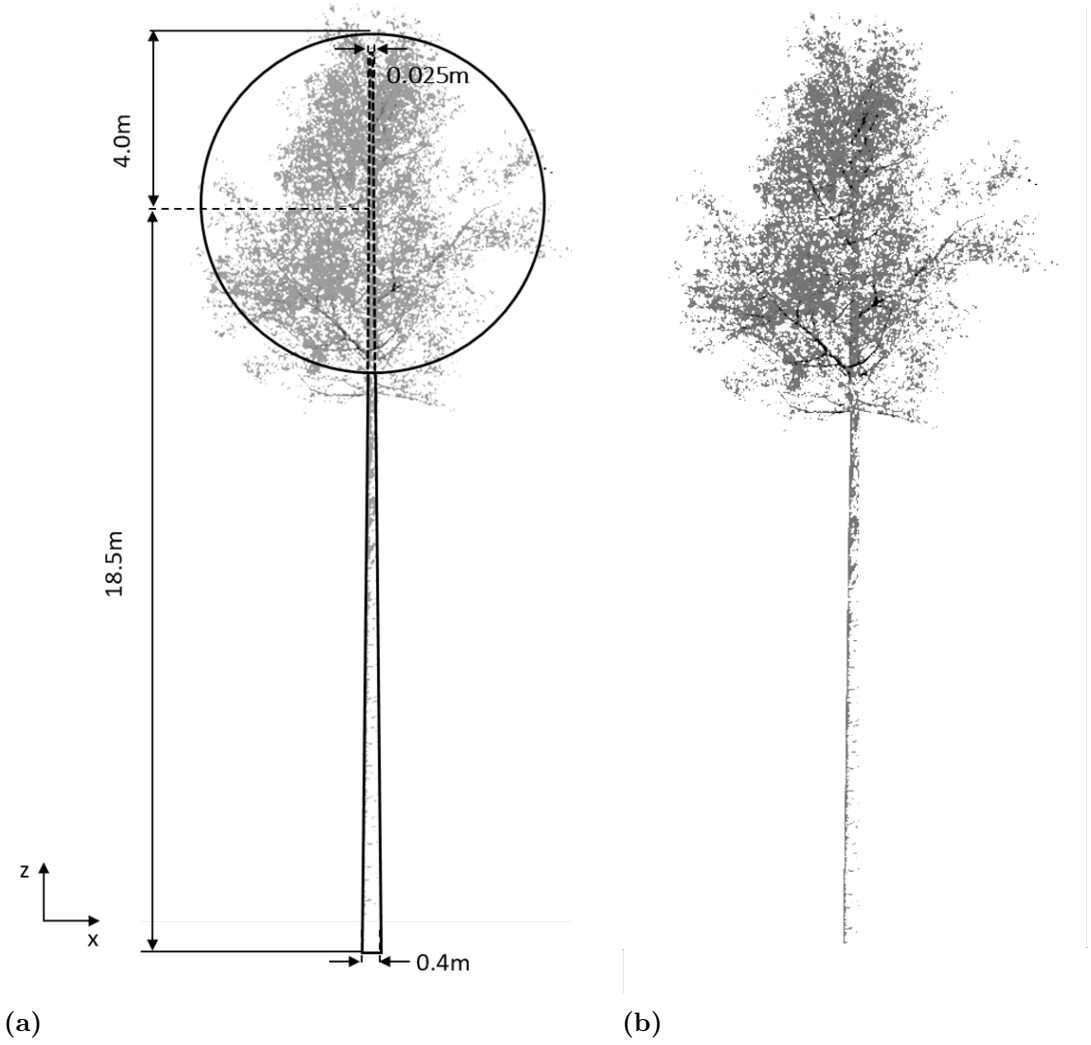

Figure 3.2: Overall form and scale of the tree representation models (a) simple-tree overlaid on reference tree geometry; (b) reference forest grown Aspen tree.

3.1.2 Branched Tree

In order to resolve the dynamics of the crown and the entire tree, the stiffness and mass-induced damping characteristics introduced by the branches must be considered. Consequently, the first-order branches of the tree are included along different levels of the main stem in BT. The branches are also considered to be tapered cylinders with taper rate similar to that of the main stem. Node diameter of the branches are considered to be half the diameter of the main stem measured at the node height of the branch. The orientation of the branches are parameterized using angles alpha (defined between axis of a branch and the positive z axis) and theta (defined between axis of a branch and the positive x axis). For the BT in the study, alpha is considered to be 45° and theta to be 0°, 90°, 180° and 270° respectively for the four branches. To position the branches along different levels of the main stem, node positions of the branches are also incorporated as a parameter. The crown is defined as in ST.

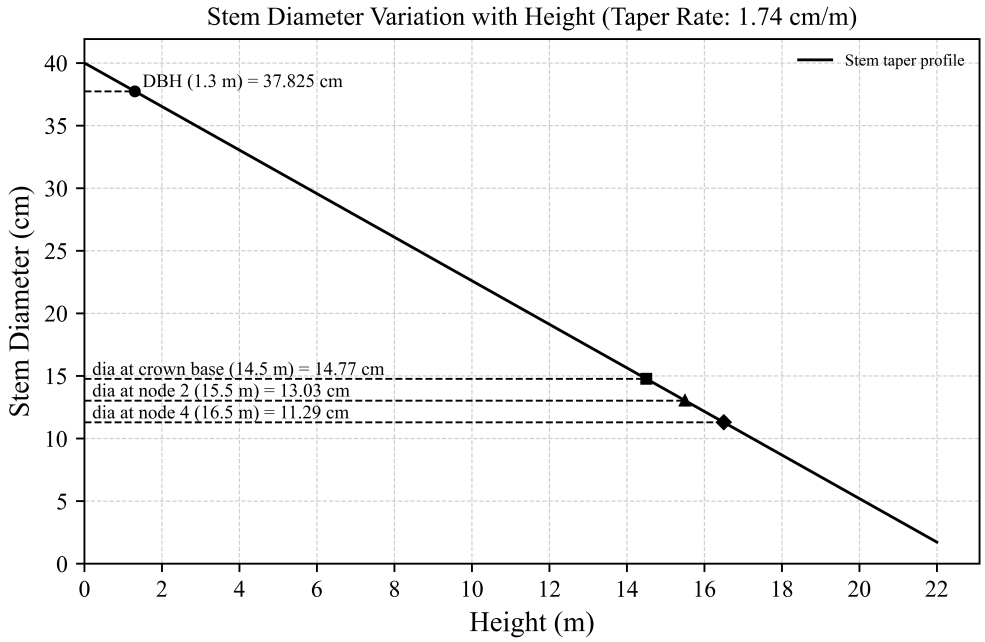

Figure 3.3: Variation of stem diameter with height for the chosen taper rate.

3.1.3 Partitioned Tree

The approximation of a continuous spherical crown restricts the degrees of freedom of the individual branches. In reality, motion of the branches are nearly independent due to morphological evolution and adaptive responses of the tree [6]. This is also vital to the tree response since, a significant amount of wind energy intercepted by the tree crown is dissipated through buffeting motion of branches [32]. Therefore, replacing the continuous spherical crown which is restrictive to the buffeting motion of the branches, partitions are introduced into the crown in PT.

The objective of having partitions in the crown is to allow a branch and its associated crown region to move independent of other branches and the main stem. A detailed discussion of partitioning procedure is given in the section 3.2.3. The overall shape of the crown is retained as spherical with the same position and diameter as in the cases of ST & BT .

3.2 Mesh Pre-Processing Steps

Having proposed the LoD, the next step was to numerically represent the different tree geometries. A single-object discretization of the tree is implemented in both FEM and CFD solvers. In this section, the steps which led to this single-object tree mesh representation are discussed.

3.2.1 Single Object Mesh Generation

The tree-mesh generation process starts with an input three dimensional, uniform and unstructured base volume-mesh with tetrahedron elements. The base mesh is defined using the overall form (volume) of the ST and was created using ANSA pre-processing software.

3.2.1.1 Marking of Wood and Crown Elements

With the single-object mesh approach, the elements with properties of wood and those of crown have to be marked. This is done with the help of an algorithm (element-locating-algorithm) to locate and mark wood elements or cells based on a geometric criteria. In summary, the geometric criteria defines the volume of the reference tree-skeleton.

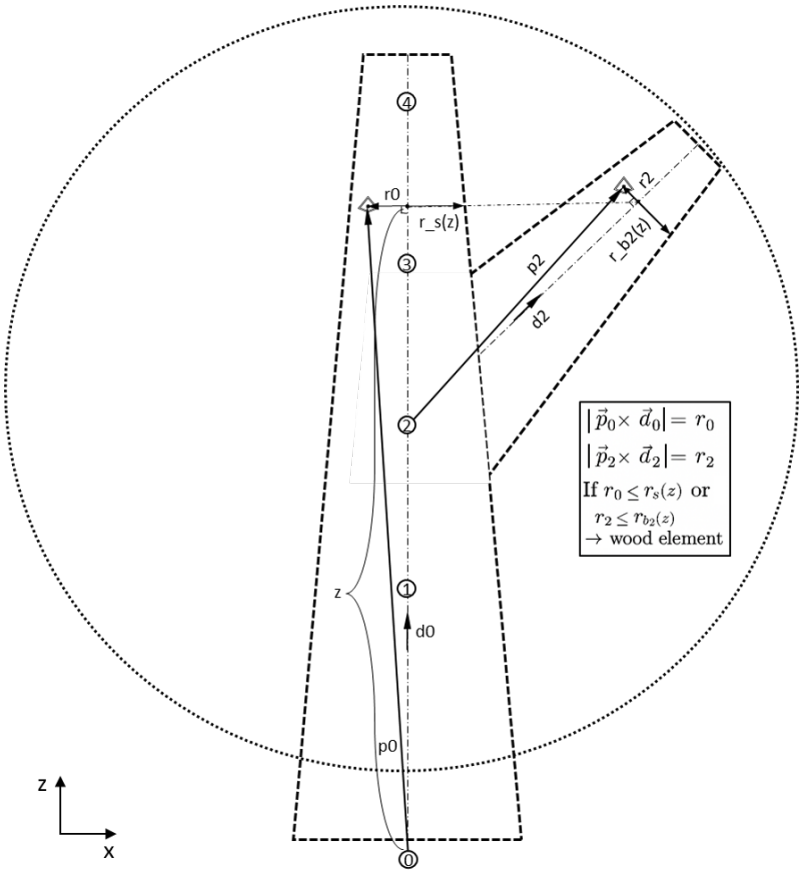

Figure 3.4: Schematic diagram of exaggerated stem region and second branch region showing parameters involved in the geometric criteria defining tree-skeleton region.

The geometric criteria is parameterized using the root diameter of the stem, the taper rate, number of branches, position of branch nodes, diameter of the branches and their orientation angles. The element-locating-algorithm scans over the base volume mesh and evaluates if the position of the center of a tetrahedron is within the tree-skeleton volume defined by the geometric criteria. If the center of the

element is within the tree-skeleton region, then the element is marked as a wood-element and the corresponding material properties are assigned.

The element-locating-algorithm using the geometric criteria works as follows. The position vectors of the center of each element with respect to the branch nodes and the root-center are found. The radial distance to the center of an element from a branch-axis or the main-stem-axis is calculated as the magnitude of cross-product between the position vectors and the unit direction vector of the branch and stem axes. The geometric criteria checks if the radial distances fall within the radius of the stem or any of the branches in order to pick the wood elements. The radius of the main stem or of the branches are defined as a function of height and taper rate. The parameters involved in the geometric criteria are schematically represented in the Figure 3.4.

3.2.2 Local Mesh Refinement Along Stem & Branches

In order to accurately resolve the stem and branches of the tree, as well as to ensure computational efficiency, local refinement of the input base-mesh along the tree-skeleton is required. This is achieved by incorporating mesh-refinement routines into the pre-processing steps. The previously defined element-locating-algorithm is modified to work as the definition of a refinement zone surrounding the stem and the branches.

The local mesh-refinement level is set using a threshold for the maximum edge length of a tetrahedron element. For those elements which fall into the refinement zone and have element edges longer than the given threshold, the corresponding elements are split into two by adding a new vertex at the midpoint of the longest edge. This also splits all other elements sharing the edge. The splitting is repeated until the threshold element size is reached. The appropriate threshold is found from the mesh study.
The wood elements marked using the element-locating-algorithm within the single-object tree-mesh, post local refinement is shown in Figure 3.5.

3.2.3 Partitioning of Tree Crown

To introduce partitions into the crown, the crown-element-set is further divided into five regions (sets) surrounding the main stem and four branches. The elements are sorted in to these five regions based on their proximity to the nearest branch or the main stem. The radial distances calculated in the geometric criteria are used for this purpose. Based on the evaluated minimum of radial distances calculated between center of the elements and axes of the stem and branches, the respective region where the element belong is identified. Accordingly, region ids are also assigned to every crown-element in the base mesh. Further, routines are added to identify neighbor elements with dissimilar region ids and thus the location of partitions.

Along the shared faces of the element pairs identified for partition, shared nodes are initially duplicated. To cut the topology along these faces, remapping of the nodes are done so that the involved element with the largest node index is assigned to use

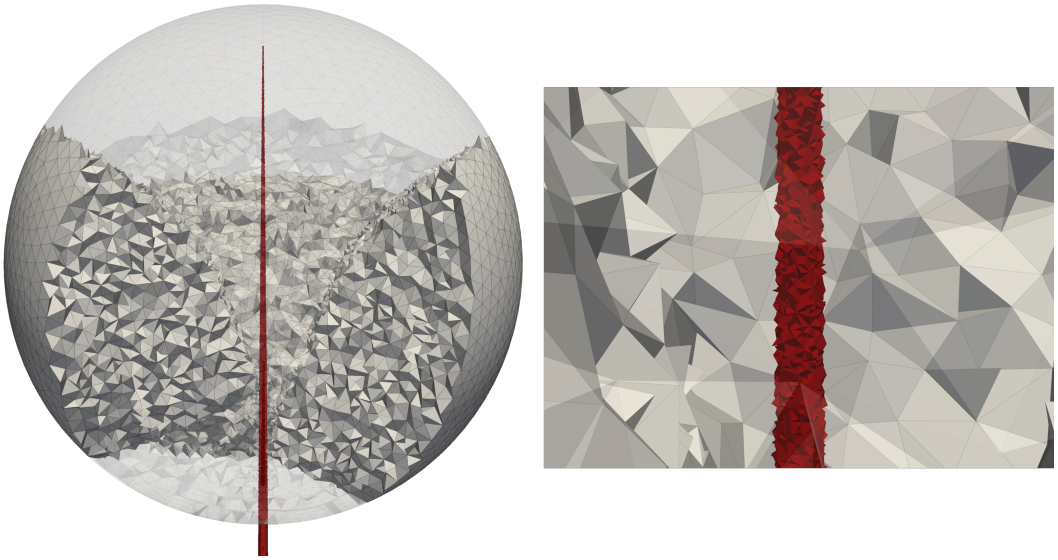

Figure 3.5: Wood elements (marked in red) resolved within the volume mesh by the element-locating-algorithm following local refinement of input mesh using a threshold maximum edge length of 3 cm. (right) Zoomed in view of resolved main-stem showing the resultant rough surface

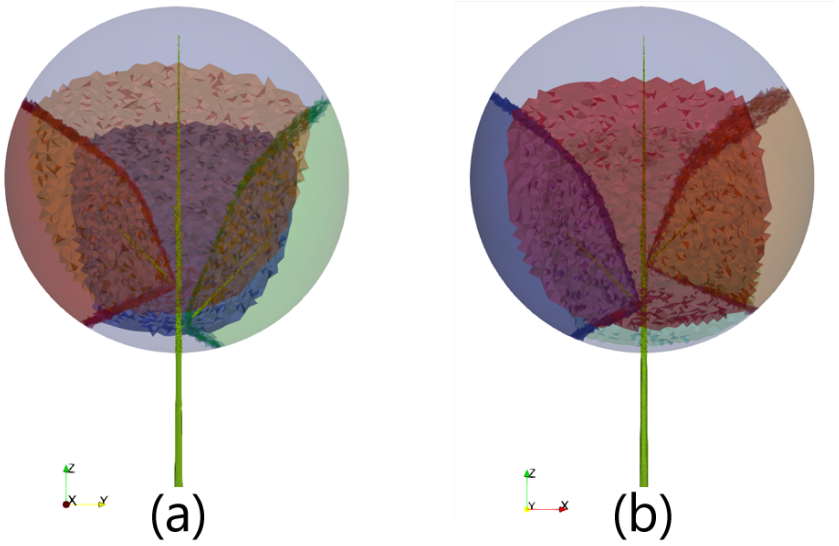

Figure 3.6: Partitioned crown elements in PT. (a) Viewed in YZ plane (b) Viewed in XZ plane

the duplicated nodes. Even though the duplicated and previously shared nodes are geometrically coincident, the remapping cuts the topology between elements. Flags are added to the partitioning routines to make sure that the partitions doesn't cut through the regions of wood elements.

By partitioning, the continuous spherical surface of the crown is modified to include the surface boundaries along the partitions. No contact constraints are defined along these new boundaries. Due to which,the regions are allowed to overlap into each other during deformation of the crown. Section views of the partitioned crown

surrounding the four branches are shown in Figure 3.6.

3.2.4 Mesh Connectivity Check

Prior to the grid independence check of the single-object tree meshes, a primary mesh performance check was also done. For this, a comparison between the aggregate of extracted wood element volume and the reference volume of tree-skeleton is made.

For coarse meshes, the extracted wood-element volume differed significantly from the reference volume. Also the entire length of the stem inside the crown was not resolved since the threshold element size was bigger than the cross-section diameter at a particular height. This caused the elements to fail the geometric criteria.

With increasing local refinement level, the percentage of extracted length and volume of the stem improved. For a particular threshold size, entire length of the stem is resolved, however the extracted volume of stem was still lower than the reference volume. A close inspection of the extracted stem elements showed discontinuities in

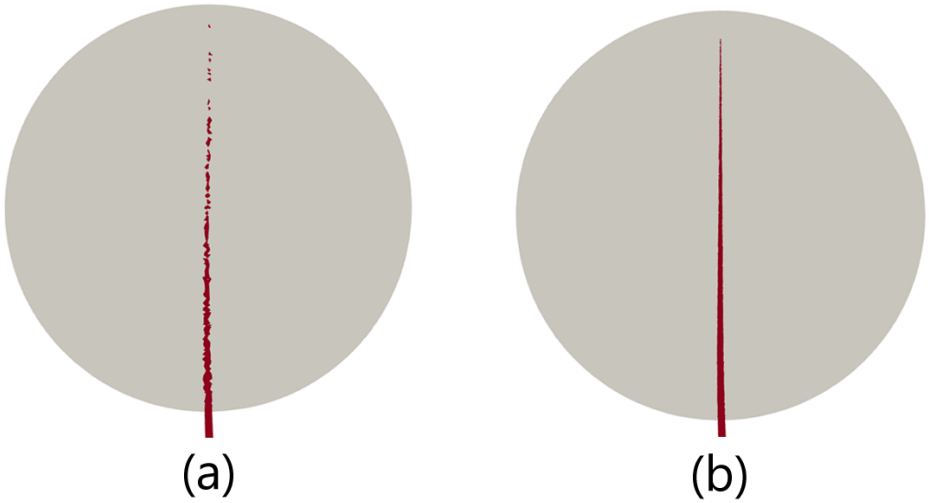

Figure 3.7: Resolved stem before and after refinement and connectivity check. (a) before refinement and connectivity check (b) after refinement and connectivity check

the stem-mesh and the missing elements were the reason for a lower magnitude of extracted stem volume.

At the upper section of the extracted stem where the cross-section diameter is small, the elements which were partially within the stem region, also failed the geometric criteria. The position of similar mesh discontinuities in the upper part of the stem varied randomly for different meshes. The discontinuities can result in occurrence of unrealistic stress and strain concentrations in the stem, and this must be avoided.

In order to eliminate the presence of mesh discontinuities in the stem, a mesh connectivity check was added as a post local refinement step. The connectivity check utilized node positions of the extracted wood-elements to evaluate connectivity with its neighbor elements. Once a discontinuity is located, the extracted wood elements

above the point of discontinuity are removed from the wood-element set and is transferred to the crown-element set.

The re-definition of wood elements which lie above the point of discontinuity to crown-element effectively reduces the overall height and volume of the stem. Hence, it is important to have sufficient local refinement proportional to the resolution of tree-skeleton that is desired. In the study the required refinement level is identified from the mesh study. The resolved stem of the ST before and after mesh refinement are shown in Figure 3.7.

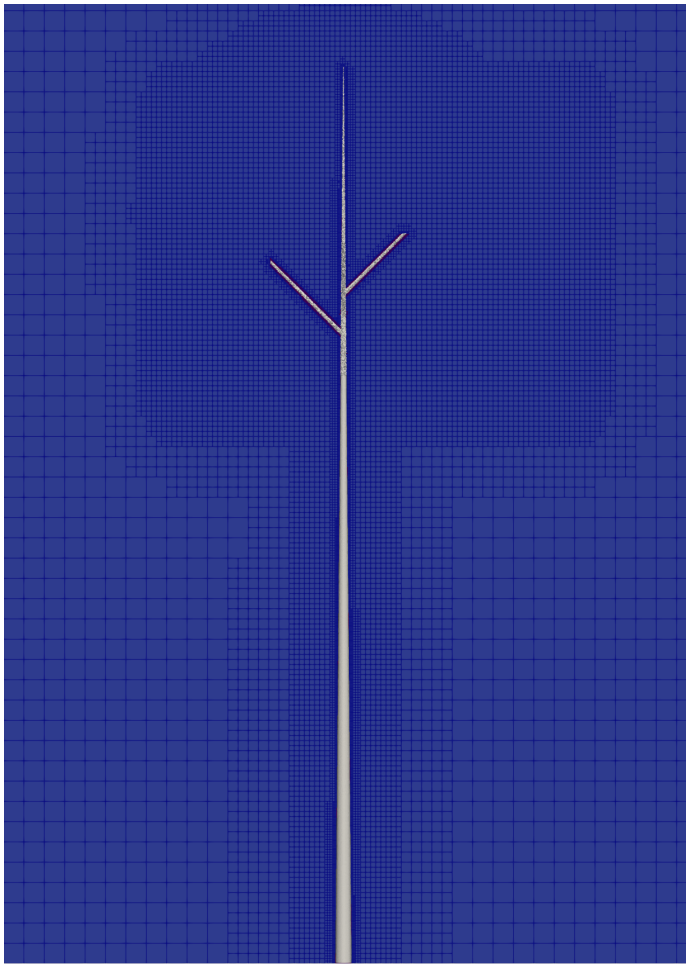

Figure 3.8: Extracted tree-skeleton surface (marked in white) inserted into cartesian mesh to perform local refinement. Viewed in X-Z plane.

3.2.5 Surface Mesh Extraction for IB-tree Local Refinement

As discussed in the introduction, we are not relying on a CAD geometry for the tree-skeleton in the study for both solvers. Also, we want to investigate the use of a fully permeable tree within the IBOFlow solver. Hence an alternative way to locate the tree skeleton and spatially define the permeability properties for stem and crown in the IBOFlow solver is used.

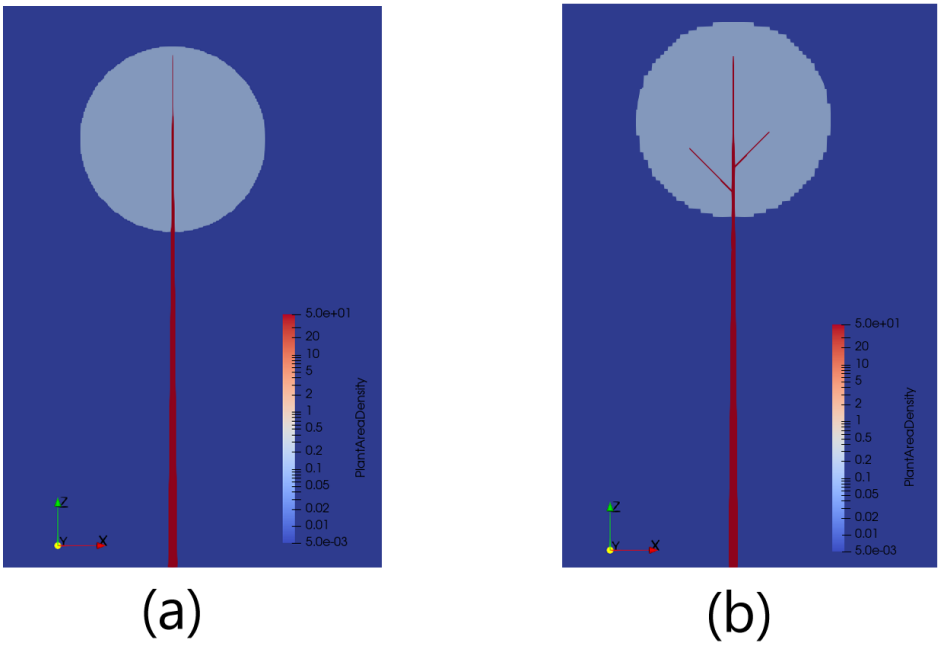

Figure 3.9: PAD distribution in IB-tree defining wood cells with PAD = 50 $m^2 \cdot m^{-3}$ and crown cells with PAD = 0.1 $m^2 \cdot m^{-3}$. (a) ST PAD distribution (b) BT PAD distribution

In the IBOFlow solver, local refinement of the tree-skeleton surface is guided by the surface mesh extracted from the FEM solver. This mesh is incorporated into the CFD computational domain as an immersed body with a free-boundary condition that remains invisible to the incoming flow. The invisible surface mesh defines the required level of local refinement, which is crucial for accurately resolving the tree-skeleton's thickness distribution and minimizing numerical diffusion during the assignment of permeability properties to the wood cells.

Figures 3.8 shows the extracted tree-skeleton surface used for local refinement. The resulting single-object ST and BT IB-trees with spatial PAD fields in IBOFlow solver are shown in Figure 3.9.

3.3 FEM Simulations in LaStFEM

Within the FEM Structural Solver (LaStFEM), our objective is to simulate the mechanical response of the tree under both static and aerodynamic loading conditions. More broadly, we aim to capture the structural behavior of real trees subjected to wind by examining the parameters that define the tree models. A critical step in achieving this is the identification of suitable material properties for the artificial crown material used in the tree-models.

3.3.1 FEM Simulation Setup

The basic setup used for the FEM simulations, investigating artificial material parameters for the tree-crown in the study are discussed in this section.

3.3.1.1 Material Properties for Artificial Crown Material

Based on the small-strain elasticity model used in the study, it is necessary to define the stiffness, density, and Poisson's ratio for the artificial crown material. Accordingly, the stiffness and density of the crown volume are specified relative to the material properties of the stem using stiffness and density ratios. The appropriate Poisson's ratio, along with suitable stiffness and density ratios for the crown material, are determined through detailed parameter studies.

Table 3.1: Material properties of Aspen wood used in the simulations.

Material Property	Value
Young's Modulus	11×10^9 Pa
Density	$440\,\mathrm{kg\,m^{-3}}$
Poisson's Ratio	0.44

The material properties of Aspen wood taken from the reference article [12] are listed in the Table 3.1. The stiffness and density ratios for the artificial crown material are defined as follows:

$$stiffness\_ratio = E_{crown}/E_{stem} \tag{3.1}$$

$$density\_ratio = \rho_{crown}/\rho_{stem} \tag{3.2}$$

3.3.1.2 FEM Boundary Conditions

For the FEM parameter studies, the aerodynamic loads on the tree under normal wind conditions were approximated as a uniform pressure force acting on the surface nodes over the windward face (surface facing the wind direction) of the tree. Assuming a steady wind speed of 10 m/s and a drag coefficient of 0.5, the average pressure on the crown surface is estimated as half of dynamic pressure equal to 30 Pa. This is an overestimate of actual pressure for a wind speed of 10 m/s, since we neglect the reduction in drag coefficient due to through flow. The root plate was defined as a fixed support.

3.3.2 FEM Mesh Study

Prior to parameter studies, the appropriate level of refinement required by the stem and crown regions of the single-object mesh must be identified. This is done using a mesh study for ST and BT geometries. The base mesh is parameterized using two variables. These are:

- maximum element size for crown elements

- maximum element size for wood elements

The size of the surface element is set as the minimum diameter limiter of the cross-section of the stem (0.025 m) and the volumetric growth rate is kept as 20%. Keeping these two parameters fixed, the maximum element sizes for crown and wood elements were varied to obtain different meshes for comparison.

3.3.2.1 Mesh Study Using ST

Two set of meshes were evaluated with ST geometry. In the initial set, for a base mesh with fixed and uniform crown element size of 0.1 m, the maximum element size of wood elements were iterated. The previously defined local refinement operation was used to set the threshold maximum wood element size. Four meshes with threshold size as 0.1 m, 0.05 m, 0.03 m, and 0.02 m were generated.

Table 3.2: Initial set of meshes comparing threshold maximum element size for wood elements

Mesh	Element Count (Million)	Max Edge Length Stem (m)	Extracted Stem Vol (%)	Extracted Crown Vol (%)	Bending Moment at Root (kNm)	Effective Stem Height (m)
M1	0.53	0.10	93.55	100.59	-23.85	18.94
M2	1.18	0.05	94.07	100.59	-24.88	21.47
M3	2.89	0.03	94.08	100.59	-24.88	21.96
M4	8.34	0.02	94.09	100.59	-24.89	22.33

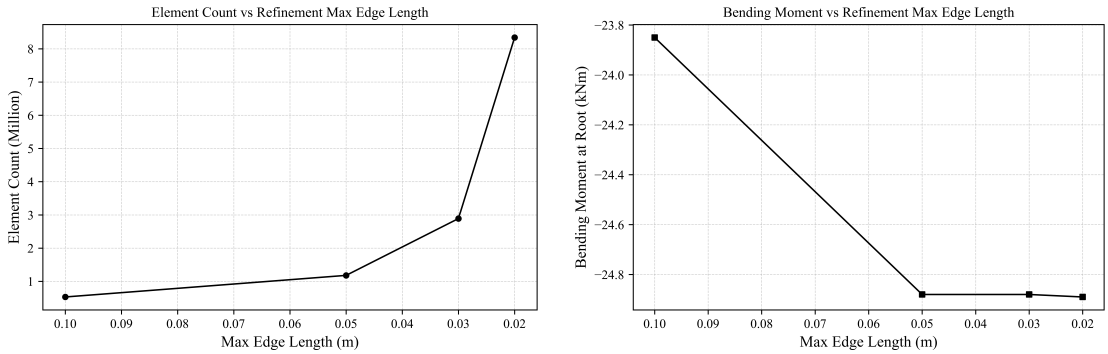

(a) Element count vs max edge length **(b)** Bending moment vs max edge length

Figure 3.10: Comparison of meshes for different max element size for stem elements.

Since the effective length of stem may vary with refinement level, the displacement over the crown can also vary significantly. Hence to monitor the convergence of mesh properties, the bending moment of the tree (effective load on the tree) measured at its root is used.

Table 3.3: Second set of meshes comparing maximum element size of the crown elements for max edge length of stem equal to 0.05 m

Mesh	Element Count (Million)	Max Edge Length Crown (m)	Extracted Stem Vol (%)	Extracted Crown Vol (%)	Bending Moment at Root (kNm)	Stem Tip Displacement (m)
M5	0.70	0.20	94.08	100.59	-27.619	1.562
M6	1.57	0.15	99.39	100.00	-27.651	1.300
M7	2.92	0.10	99.39	100.00	-27.651	1.300

Variation in bending moment seems to converge after mesh $M2$. And visual comparison between $M2$ and $M3$ also showed that the thickness distribution of effective stem identified by the geometric criteria seems to follow the reference stem. The

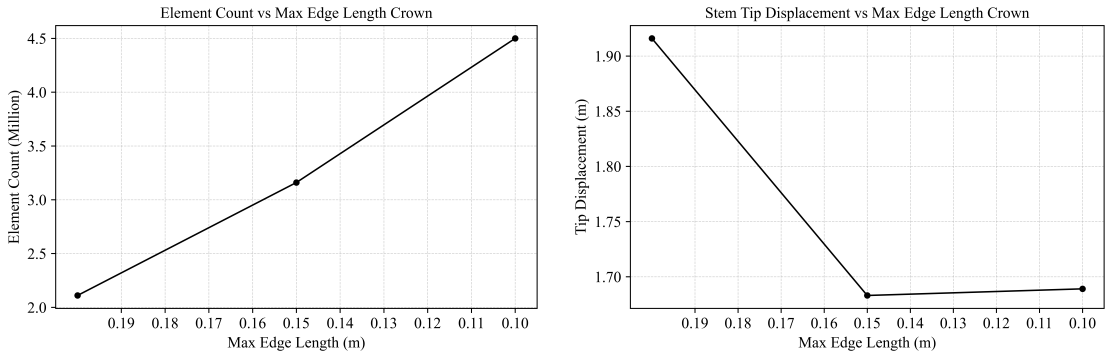

(a) Element count vs max edge length. **(b)** Tip displacement vs max edge length.

Figure 3.11: Comparison of meshes for different max element size for crown elements.

comparison of effective extracted volume and actual tree volume until the point of discontinuity is also reported in the table showing initial mesh study results Table 3.2. From the initial mesh study results, mesh $M2$ with max edge length 0.05 m was selected for further studies.

In the second set of meshes, the maximum element size possible for the crown elements is determined. The converged maximum wood element size from the initial set was used in these cases. Three meshes with maximum crown element sizes 0.2 m, 0.15 m and 0.1 m were compared. The tip displacements of the effective stem were monitored for mesh convergence. The results from the second set are given in Table 3.3.

Based on the convergence in tip displacement and root bending moment, mesh $M6$ with max edge length for crown elements equal to 0.15 m and max edge length for stem element equal to 0.05 m was selected as the final mesh for FEM parameter study.

Table 3.4: Second set of meshes comparing maximum element size of the crown elements using BT for max edge length stem equal to 0.05 m

Mesh	Element Count (Million)	Max Edge Length Crown (m)	Extracted Stem Vol (%)	Extracted Crown Vol (%)	Bending Moment at Root (kNm)	Stem Tip Displacement (m)
M5	0.83	0.20	95.50	100.59	-27.612	1.562
M6	1.70	0.15	100.80	100.00	-27.646	1.300
M7	3.03	0.10	100.80	100.00	-27.649	1.299

3.3.2.2 Mesh Study Using BT

Using the defined refinement routines and mesh connectivity checks, the two set of cases were re-evaluated for the BT case. The results underlines the convergence of the selected mesh parameters as in $M6$. The results for BT are shown in Table 3.4.

3.3.3 FEM Parameter Study

To re-iterate, the two-fold objective of the FEM parameter studies are:

1. Identify the relevant material parameters for the artificial crown material.
2. Find the bounds for these material parameters that can generate the expected physical character of a real tree.

Throughout the parameter study simulations, the ST geometry is used and material properties of the wood elements are kept fixed.

3.3.4 Results & Discussions from FEM Parameter Study

3.3.4.1 Stiffness Ratio

The primary response of the tree crown under wind load, happens as the deformation of the outer region of the crown. The local deformations in the crown surface results in overall streamlining of it. The stiffness properties of the simplified spherical crown should be in a range that facilitates this streamlining effect. Therefore, identifying appropriate stiffness ratio for the crown elements was the initial objective in the FEM parameter studies.
A uniform stiffness ratio was used across the crown volume initially. The order of magnitude of the stiffness ratio was iterated between 10^{-1} and 10^{-8}, while keeping density ratio and Poisson's ratio fixed at magnitudes 10^{-8} and 0.44 respectively. The choice of density ratio to be 10^{-8} was to neglect the contribution of weight induced deformation into the streamlining. Also Poisson's ratio was set to match the Poisson's ratio of wood to keep the crown nearly incompressible during streamlining. The Poisson's ratio was not set to 0.5 to avoid singularity of having an infinite

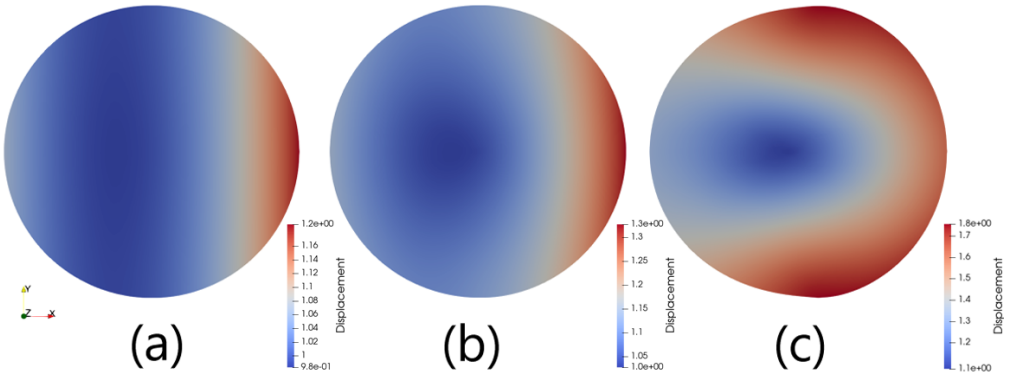

Figure 3.12: Deformation of crown viewed in $X-Y$ plane passing through center of the crown. (a) stiffness ratio = 10^{-6} (b) stiffness ratio = 10^{-7} (c) stiffness ratio = 10^{-8}

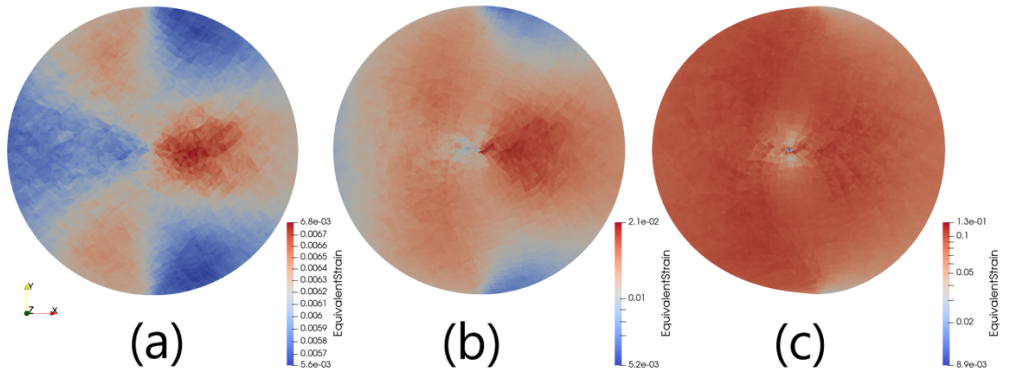

Figure 3.13: Equivalent strain plots of crown viewed in $X-Y$ plane passing through center of the crown. (a) stiffness ratio = 10^{-6} (b) stiffness ratio = 10^{-7} (c) stiffness ratio = 10^{-8}

bulk modulus. The observed deformation across the crown surface as well as the equivalent strain fields are shown in Figures 3.12 and 3.13 respectively.
With decreasing stiffness ratio and effective stiffness of crown elements, local deformations started to appear on the crown surface. For stiffness ratio 10^{-7} the streamlining effect starts to be evident and is significant for 10^{-8} case. Thus its inferred that the stiffness ratio has to be lowered to the order of 10^{-8}, in order for the crown surface to show significant deformation under normal wind conditions.

It is also important to remark that, with increasing resolution of the stem where we include the higher order branches, the resulting crown will be composed more of foliage and voids. The change in composition of the crown must be considered in the choice of stiffness ratio and other properties for the BT.

Based on the equivalent strain plots in Figures 3.13 and 3.14, very high strain levels are observed in crown elements near the stem. This is attributed to the high accumulated pressure acting on these regions and must be mitigated. To reduce overall strain levels in the crown while still capturing the deformation of the crown

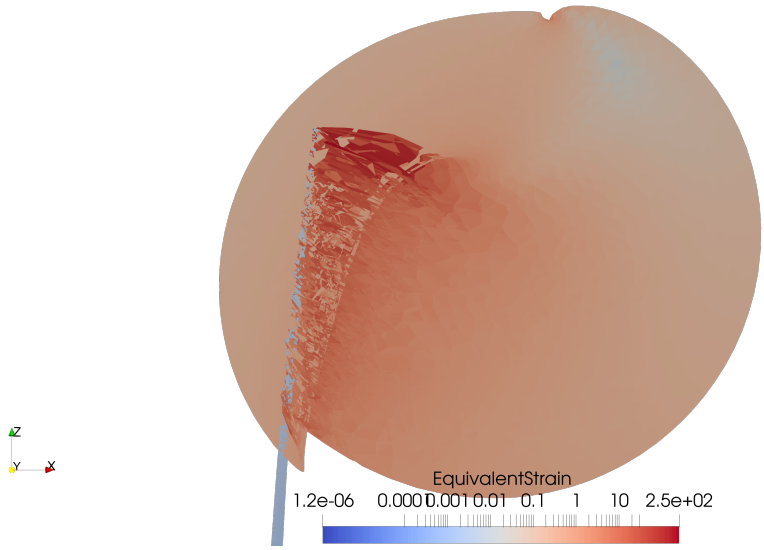

Figure 3.14: Equivalent strain plot of crown section viewed in X-Z plane passing through center of the crown for stiffness ratio = 10^{-8}, density ratio = 10^{-8} and Poisson ratio = 0.44

surface, a non-uniform stiffness ratio is required. This is implemented through a spatially varying (field) definition of the stiffness ratio, which will be discussed in the following section.

3.3.4.2 Stiffness Ratio Field

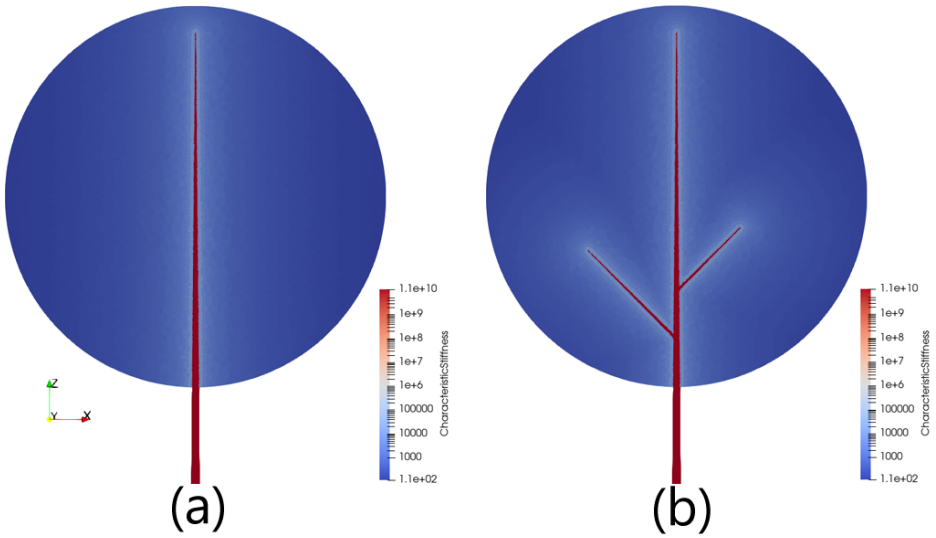

Figure 3.15: Characteristic stiffness of elements across the discretized crown volume consisting of 50 levels (a) ST stiffness field (b) BT stiffness field

Like we discussed in the beginning of section 3.3.4.1, compared to the deformation of the crown elements along the crown surface, crown volume close to the stem are less deformed. It is observed in a real tree that the crown volume close to the stem

and at the core of the crown, follow the stem during its displacement rather than undergoing significant deformation. Hence it is reasonable to assume that the crown elements close to the stem are stiffer than those at the surface in order to be able to resist deformation. The degree of deformation in crown elements is observed to increase as we move radially outward across the crown.

Accordingly, a spatial stiffness ratio field was defined to assign stiffness to crown elements based on their distance from the nearest stem or branch. The crown volume was discretized into multiple levels, with the zeroth level being closest to a stem or branch, and each level assigned with a unique id. The stiffness ratio was then varied across these levels according to the minimum of evaluated distances to the stem or branch axes. (The specific discretization approach was because of a current limitation in LaStFEM restricting element-wise property definition.)

The growth of the stiffness ratio from its value at the crown surface to the value at the zeroth level was defined to follow an inverse relationship with the radial distance from the stem axis. Assuming a cylindrical iso-surface around the central stem axis, internal stresses were approximated as pressure applied over the surface of this cylinder. Under this assumption, the internal stress increases inversely with radial distance from the stem axis. To counterbalance this increase, the stiffness ratio is scaled proportionally from its base value at the crown surface.

For cylindrical iso-surface assumption:

$$P_{iso} = \frac{F_{aero}}{2\pi r_{iso} l} \tag{3.3}$$

For spherical iso-surface assumption:

$$P_{iso} = \frac{F_{aero}}{4\pi r_{iso}^2} \tag{3.4}$$

For more complex tree geometries with extensive branching, a spherical iso-surface approximation can be more appropriate than a cylindrical one. In such cases, the growth of the stiffness ratio can be considered to follow an inverse-square relationship with radial distance.

The gradual decrease in characteristic stiffness of the crown elements with respect to radius, helps to avoid high strain levels across the volume of the crown and to localize large deformations along the outer regions of the crown. The equivalent strain in crown elements across the different levels achieved using the field definition of stiffness ratio are shown in Figure 3.16. In the plots, moderately high but localized strain is observed at elements close to the tip of stem and branches. However the average equivalent strain values across the volume range between 5 to 10 percent.

By defining stiffness ratio as function of the proximity to nearest stem or branch, a more robust distribution of stiffness is achieved in the crown. Depending on the composition of the crown, the order of decay as well as magnitude of stiffness ratio at the surface of the crown can be easily modified with this approach. Hence instead of uniform stiffness ratio definition, hereafter the simulations were carried out using stiffness fields.

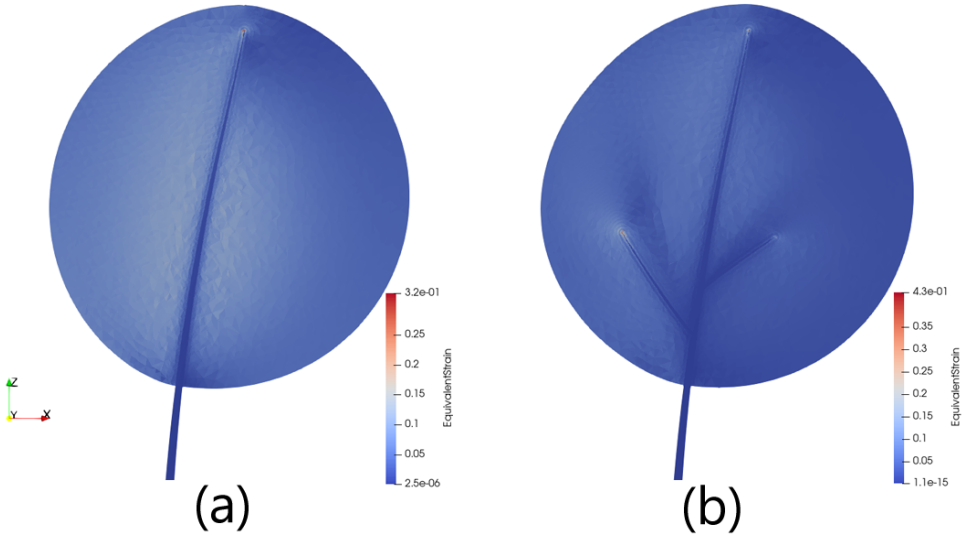

Figure 3.16: Equivalent strain plots in deformed state of elements across the discretized crown volume consisting of 50 levels (a) ST stiffness field (b) BT stiffness field

3.3.4.3 Poisson Ratio

The second key parameter affecting the overall deformation of the crown is the Poisson's ratio. In the set of cases discussed in section 3.3.4.1, we used a Poisson ratio of 0.44. This makes the crown nearly incompressible for wind loads and this is not the case for an actual tree. The morphology of a tree crown allow it to undergo compression to certain limit. The presence of voids and the independent nature of motion of the branches, makes this compression to occur without lateral expansion or contraction. Resolving this behavior of the crown was the primary motivation to investigate the influence of Poisson's ratio in crown deformation.

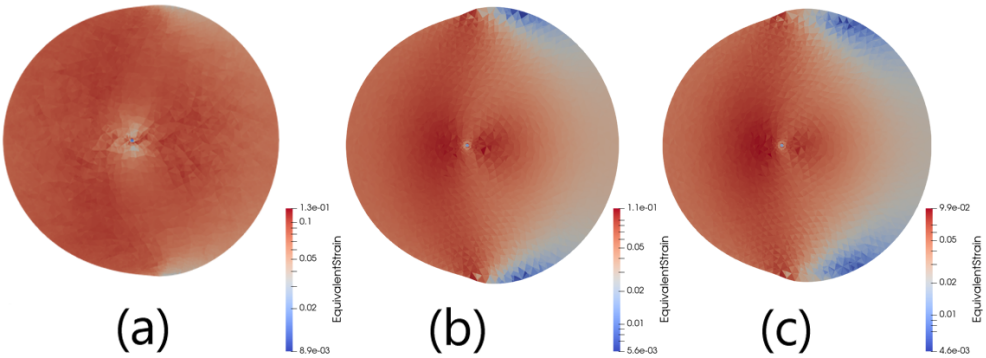

Figure 3.17: Equivalent strain plots of crown viewed in $X - Y$ plane passing through center of the crown. (a) Poisson's ratio = 0.44 (b) Poisson's ratio = 0.0 (c) Poisson's ratio = -0.2.

Keeping the stiffness ratio and density ratio at 10^{-8}, the Poisson's ratio of the crown elements was iterated between 0.44 and -0.2. An element with Poisson ratio close

to 0.5, behaves like a rubber while a negative Poisson ratio would mean lateral contraction under compression (expansion under tension). However Poisson ratio of magnitude 0.0 allows compression without lateral expansion or contraction. This is similar to response observed in porous materials as well as in certain honeycomb structures [25, 7].

The equivalent strain plot of the deformed crown cross-section for Poisson's ratio 0.44,0.0,-0.2 are shown in Figure 3.17. For decreasing Poisson's ratio, the lateral expansion (bulging) of the crown decreased. And for Poisson's ratios 0.0 and below, some amount of compression followed the streamlining deformation. The area of cross-section of the crown is also observed to be smaller in the case of zero Poisson's ratio than in the case of 0.44. Between Poisson's ratio 0.0 and negative values, variation in deformation was minimal. This might be because of the nature of the loading which is uniform across the crown surface. The Poisson's ratio 0.0 was selected for future cases since it aligned with the expected behavior in actual trees.

Even though the average strain levels in the crown is higher than accepted strain levels for small strain elasticity model, the choice of Poisson's ratio zero for the crown allows to decouple the strains and this can improve stability of the FE solver. The accuracy of resolving local deformation in the crown using small strain elasticity model has to be investigated. However, the objectives of streamlining of the crown is achieved with the selected Poisson's ratio and stiffness distribution. This will ensure realistic variation of aerodynamic load in flow simulations. Since the strain levels in the stem are within the limit of 0.05%, the primary bending response of the tree is accurately resolved using the selected material models.

3.3.4.4 Density Ratio

To accurately predict the overall response of the crown, a realistic representation of crown mass is essential. After establishing the stiffness and Poisson's ratio for the crown elements, a homogenized bulk density for the crown was initially estimated. Average total mass and foliage mass fraction (leaves and twigs) for an aspen tree were taken from reference [17]. For an average total fresh weight of 636 kg, the foliage mass fraction was taken as 0.3, giving a crown mass of approximately 190.8 kg. Given a crown volume of 268 m^3 (from the ST crown geometry), this corresponds to a bulk density of 0.712 kg/m^3 and a resulting density ratio of 0.00162. For the ST model, the volume of wood is approximately 0.96 m^3. Using a reference wood density of 440 kg/m^3 for aspen, the total wood mass sums to 613.2 kg. This closely matches the average tree mass referenced in the study, supporting the accuracy of the estimate.

Since the density ratio is derived solely from the foliage mass fraction, the value of 0.00162 is used as a reference for the parameter study. Using this estimated bulk density and corresponding density ratio, the crown's deformation by self-weight was simulated. The resulting deformation is shown in Figure 3.18.

The results reveal significant deformation due to self-weight. The crown, initially spherical, deforms into an oval shape, and the stem and branches exhibit noticeable bending. This contradicts the assumption that, in the absence of wind, the crown

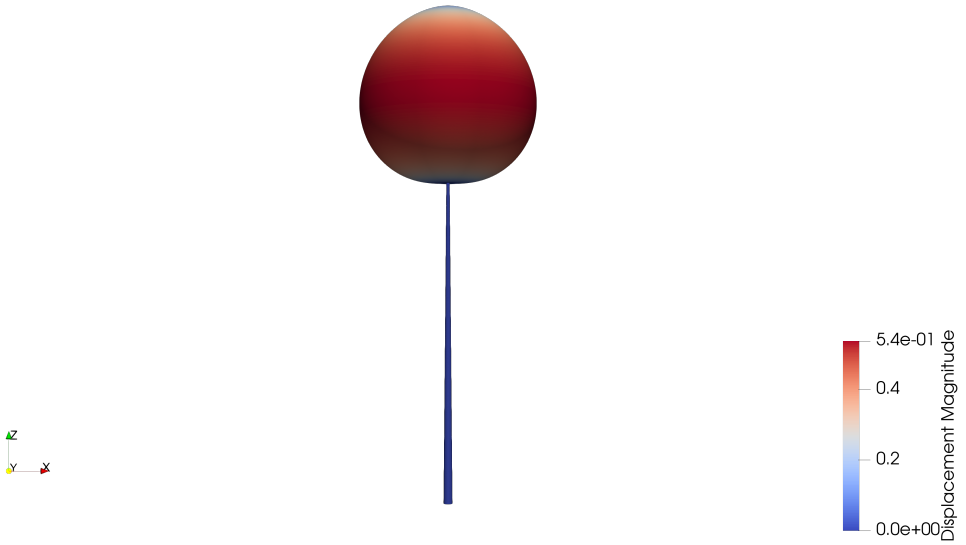

Figure 3.18: Deformation under self-weight of the crown viewed in the X–Z plane for the estimated density ratio of 0.00162, (stiffness ratio = 10^{-8}, Poisson ratio = 0.0).

maintains a spherical equilibrium geometry. The approximated tree skeleton is unable to support the estimated crown mass under gravity alone.

It was therefore concluded that a realistic density ratio must incorporate actual thickness variations across the tree skeleton. To preserve the spherical no-wind geometry and ensure that all deformation arises solely from aerodynamic loading, the crown density ratio was excluded from the simulation. Instead, a very low density ratio of 10^{-8} was assigned to the crown, effectively rendering it massless.

To still account for the crown's mass and its damping contribution, the estimated crown mass was redistributed across the stem and branches. This assumes a balanced mass distribution, justified by the hypothesis that trees optimize their structural mass distribution during growth [26].

3.3.5 Base Case Deformations in ST, BT & PT

To conclude the parameter studies in LaStFEM, pure FEM simulations were performed on ST, BT, and PT using a consistent set of established parameters. The common parameters applied across all three cases include:

- Stiffness ratio = 10^{-8}
- Poisson ratio = 0.0
- Density ratio = 10^{-8}

A comparison of the deformation plots reveals that, relative to ST, the crown in BT undergoes less compression. This indicates that the added structural stiffness provided by the branches plays a significant role in resisting deformation.

Within the PT, an asymmetric deformation is observed. Compared to the windward partition zone of the crown, the lateral and top partitions experience greater dis-

placement due to pressure loading. The windward zone undergoes less deformation, primarily because of the reduced exposed area and the corresponding decrease in bending moment, which together diminish the effective wind load acting on that region. Also as expected, the partitions are facilitating overlap of the crown regions.

Across all three cases, the crown exhibits streamlining accompanied by primary bending deformation. By incorporating the surrounding pressure field from CFD simulations, the one-way coupled FSI simulations will provide a more realistic representation of the crown's deformation behavior.

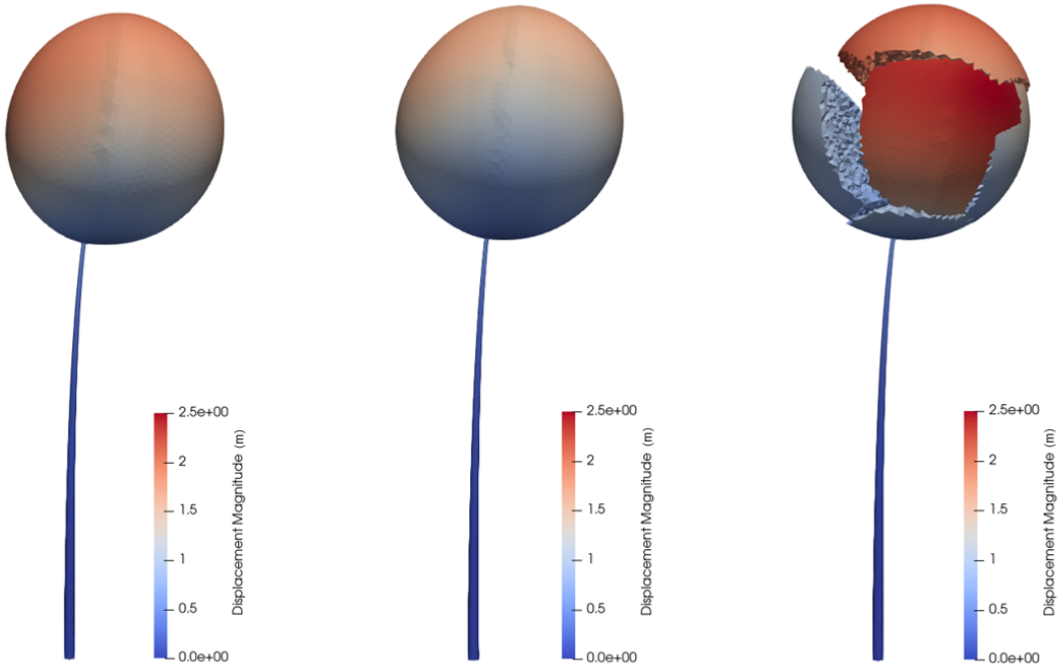

(a) ST **(b)** BT **(c)** PT

Figure 3.19: Pure FEM base case deformations in ST, BT, and PT, viewed in the X–Z plane.

3.4 CFD Simulations in IBOFlow

In the IBOFlow solver, the flow field over and through the tree is computed. From the flow field, the aerodynamic loads acting on the tree can be found. Similar to the single-object tree representation in structural solver, a single IB-object tree with internal cells having varying permeability properties across wood and crown regions is defined in the flow solver. This is in contrast to the approach where a permeable fluid-object crown is spatially coupled to a solid-object stem.

Instead of fully resolving the flow through the tree crown, permeability model based on source term modification are used to induce variation in flow properties. In a

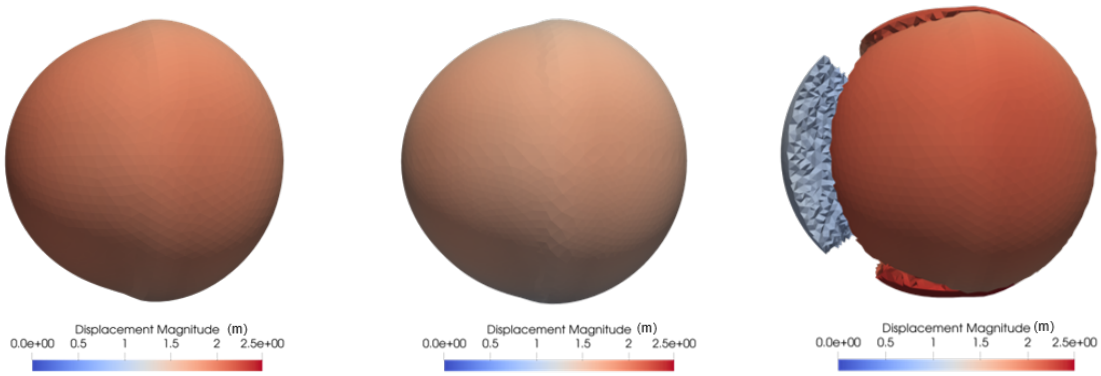

(a) ST (b) BT (c) PT

Figure 3.20: Pure FEM base case deformations in ST, BT, and PT, viewed in the X–Y plane.

similar way, the source terms are modified in the wood cells in order to obstruct the flow through them. Using a relatively higher value of PAD than the realistic PAD values used in the crown, the incoming flow is obstructed in the wood cells. Appropriate PAD values for both wood and crown regions are identified through parameter studies.

3.4.1 CFD Simulation Setup

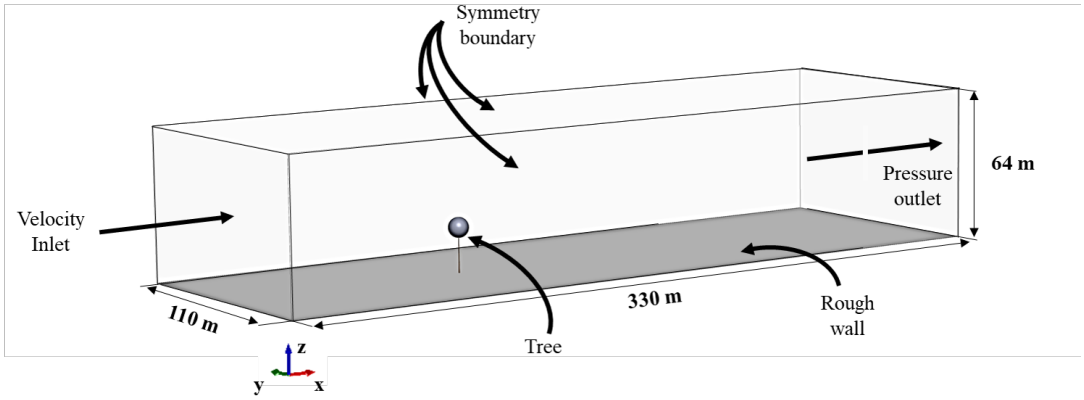

Figure 3.21: Overall dimensions of computational domain in CFD simulations with boundary conditions used.

The basic setup used for CFD simulations in the IBOFlow solver are discussed in this section. The computational domain is defined according to the best practice guidelines discussed by Blocken et al.[3]. The inlet conditions follow the definition of standard ABL flow [20, 42]. The ground is defined as a rough wall with aerodynamic roughness height chosen as 0.0018 m (flat terrain with no obstacles). The average wind speed at the crown level is approximately 12 m/s, according to the generated inlet velocity profile. The sides and top boundaries of the domain are defined using

symmetry boundary conditions. At the outlet, a pressure outlet condition is used. The overall dimensions of computational domain is given in figure 3.21.

The log-law inlet velocity profile, inlet profiles for turbulent kinetic energy and dissipation rate generated according to the standard ABL flow wall functions discussed in 2.3.4 are given in Figure 3.22.

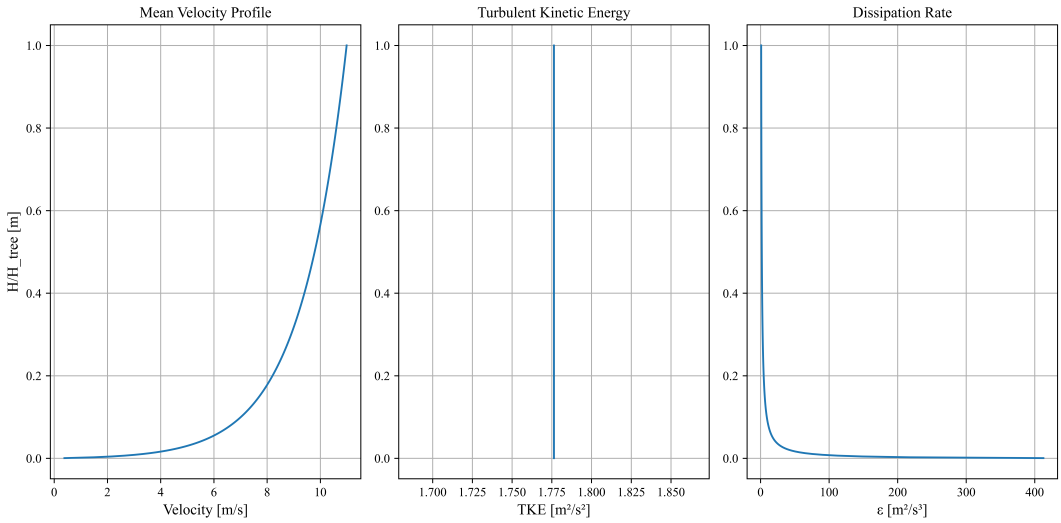

Figure 3.22: Velocity, turbulent kinetic energy, dissipation rate inlet profiles generated according to standard ABL wall functions.($z_0 = 0.0018$, $u^*_{ABL} = 0.73$ m/s, $\kappa = 0.42$).

To model the through flow in crown, the permeability model discussed by Sogachev et al. [34], with coefficients proposed for a solitary tree by Dellwik et al. [8] are used.

Based on the measurements of drag coefficient by Dellwik et al, the drag coefficient in the source term for crown cells was set to be fixed and equal to 0.25. For the wood cells, drag coefficient was set equal to one. This makes the source terms to be a function of PAD alone. Previous validation studies (not part of this work) have shown good performance of the model working with k-ϵ turbulence model. Hence the simulations in the study are conducted using it.

3.4.2 CFD Mesh Study

For the mesh study in IBOFlow, two set of cases were conducted. The initial set of meshes focused on identifying the global mesh parameters for the exterior cells of the IB-tree as well as getting a reference for the forces over tree stem. The mesh parameters included global refinement levels and local wake refinements for the tree-object. To this purpose, a benchmark case using solid object stem of ST was conducted. For different mesh refinement levels, the overall pressure force, calculated by integrating over the surface of the IB-tree-stem were monitored. The force comparison for different mesh levels from the initial set of cases are shown in Table 3.5.

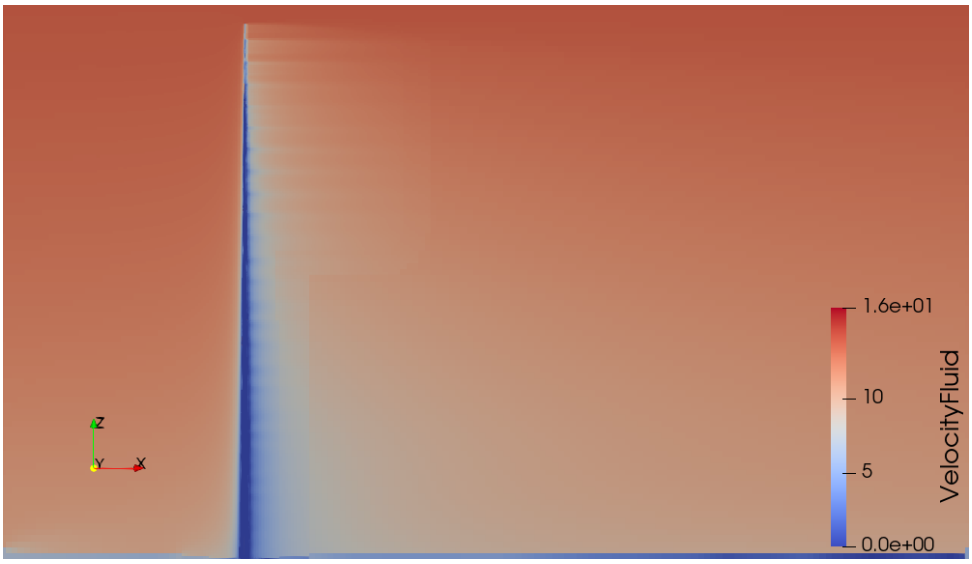

(a) Velocity field for ST solid stem reference case

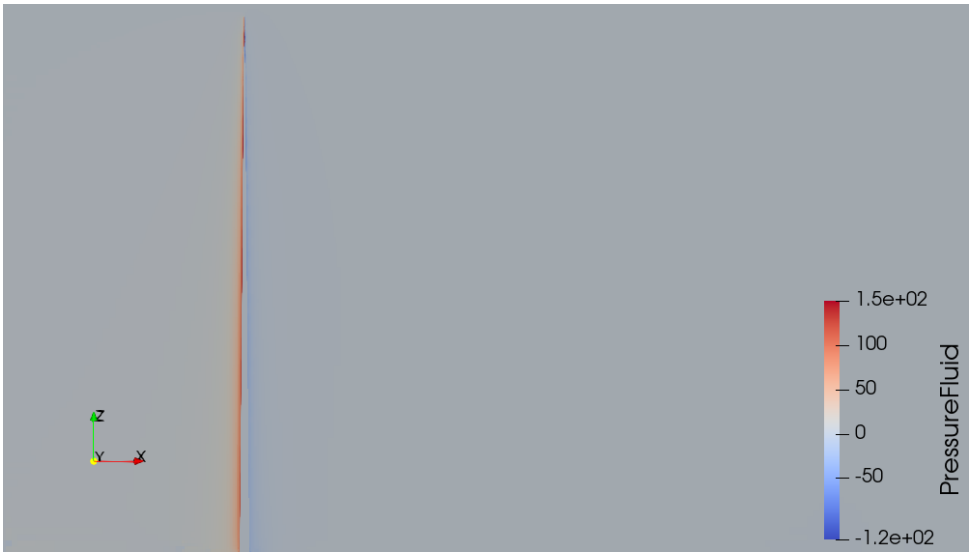

(b) Pressure field for ST solid stem reference case

Figure 3.23: Velocity contour plots for the benchmark cases using ST solid stem and global mesh parameters of Mesh M3

The velocity and pressure fields plotted along the $X-Z$ plane passing through center of the solid stem for ST are shown in Figure 3.23. From the plots, a peculiar pattern is observed in the wake of the tree. This pattern resembles the 2D snapshot of the wake field, for a tapered cylindrical body kept in cross flow [21, 37]. The reducing amplitude across the height corresponds to the reducing characteristic length scale (cross-section diameter) of vortices shed by the cylinder.

The overall pressure force calculated over the stem seems to converge from M2. Also, the global mesh parameters and the level of wake refinement used for mesh M2 seems to resolve the mean wake field with sufficient accuracy and therefore, it is followed in further cases.

Table 3.5: Mesh study using solid-object stem of ST

Mesh	Wake Cell Size (m)	Streamwise Force Component ST (kN)
M1	0.031	0.4959
M2	0.016	0.4731
M3	0.008	0.4737

(a) Velocity field for BT using mesh M4

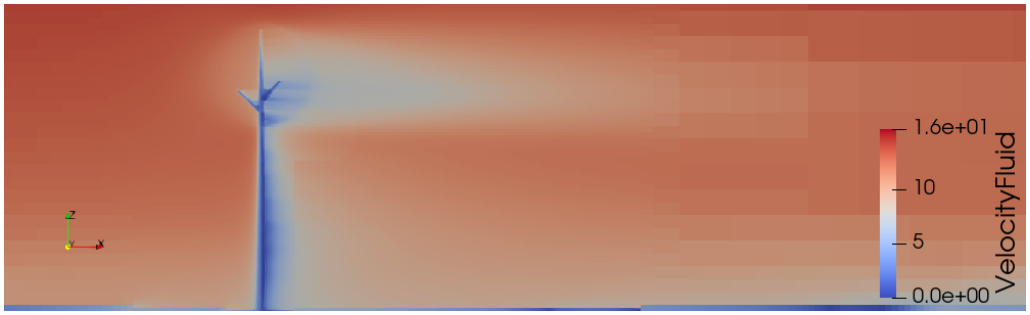

(b) Velocity field for BT using mesh M5

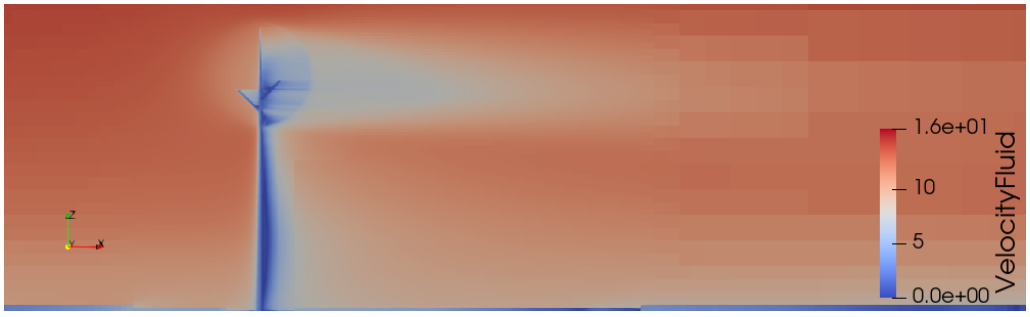

(c) Velocity field for BT using mesh M6

Figure 3.24: Velocity contour plots for different mesh resolutions of IB-tree with PAD for wood cells = 50 $m^2 \cdot m^{-3}$ and PAD of crown cells equal to 0.1 $m^2 \cdot m^{-3}$.

The second set of meshes were aimed at identifying the refinement levels required for the internal cells of the IB-tree as wells for resolving the branches of BT. Here actual PAD based fully permeable IB-tree with PAD of the stem equal to 50 $m^2 \cdot m^{-3}$ and PAD of crown cells equal to 0.1 $m^2 \cdot m^{-3}$ is used. Three meshes with varying

(a) Pressure field for BT using mesh M4

(b) Pressure field for BT using mesh M5

(c) Pressure field for BT using mesh M6

Figure 3.25: Pressure contour plots different mesh resolutions of IB-tree with PAD for wood cells = 50 $m^2 \cdot m^{-3}$ and PAD of crown cells equal to 0.1 $m^2 \cdot m^{-3}$

local refinement level for the tree-skeleton surface was generated and compared. The overall pressure force acting on the IB-tree surface measured for these three meshes are shown in Table 3.6. The corresponding velocity and pressure fields are shown in Figures 3.24 and 3.25.

Analyzing the result plots, wake field of the main-stem and the branches are well resolved with mesh M6. This is evident with a comparison of wake near lower part of the stem as well as directly behind the branches. The forces obtained for the ST stem indicate the onset of convergence starting from mesh M5. Therefore mesh refinement properties of M6 is followed in CFD parameter study meshes.

Table 3.6: Mesh study using fluid-object IB-tree of ST with PAD-wood = 50 $m^2 \cdot m^{-3}$, PAD-crown = 0.1 $m^2 \cdot m^{-3}$

Mesh	Internal Cell Size (mm)	Streamwise Force Component ST (kN)	Streamwise Force Component BT (kN)
M4	1.95	1.157	1.739
M5	0.97	1.220	1.895
M6	0.65	1.250	2.026

3.4.3 CFD Parameter Study

As discussed before, the objective in CFD parameter studies is to identify the appropriate level of permeability defined by PAD, for wood and crown cells. Thus the key parameters investigated in IBOFlow parameter study simulations are,

- PAD for wood cells (PAD-wood)
- PAD for crown cells (PAD-crown)

The PAD for the wood cells should allow to mimic the obstruction of flow caused by a solid stem while PAD for crown cells should resolve the through flow properties in the crown. Therefore, two fold simulations are conducted here.

3.4.4 Results & Discussions from CFD Parameter Study

3.4.4.1 PAD for Wood Cells

Table 3.7: Results from parameter study of PAD value for wood cells using ST stem

PAD-wood ($m^2 \cdot m^{-3}$)	Velocity Inside Stem (m/s)	Streamwise Force Component (kN)
10	4.86	0.326
30	2.97	0.422
50	2.30	0.459
70	1.94	0.478
90	1.54	0.470

In the first set of cases, Plant Area Density of Wood Cell (PAD-wood) is established. For this, PAD value for the crown cells is set to zero. Using ST fluid-object stem and keeping the drag coefficient equal to one, PAD-wood in the permeability model was iterated in the cases. For different PAD values, the overall pressure force acting over the permeable ST-stem was monitored.

The iterated PAD-wood values and the corresponding forces on the permeable stem are presented in Table 3.7. The variation of forces and velocity measured inside the stem at a distance of 1 m from the ground are plotted in the Figure 3.26.

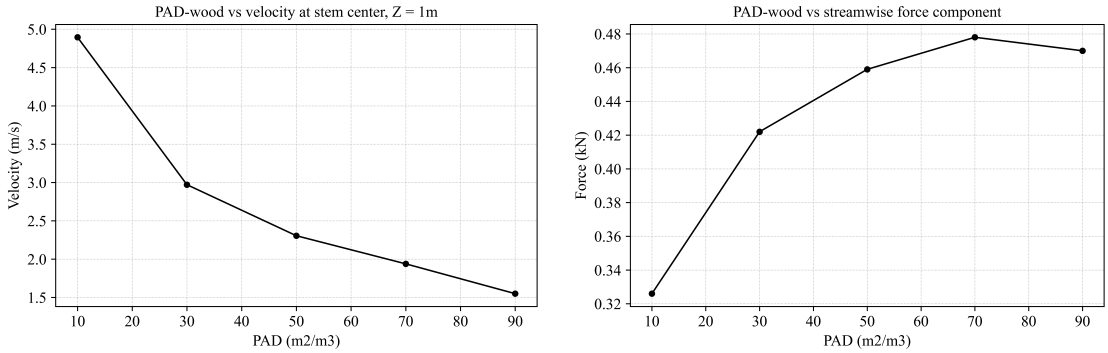

(a) Through-flow velocity variation **(b)** Pressure force component variation

Figure 3.26: Through-flow velocity and streamwise pressure force component variations from PAD-wood parameter study results

Comparing the results for solid stem and the fluid-object permeable stem, permeable stem does have some amount of through flow in it. The velocity of this through flow is decreasing with increasing PAD value.

Comparing the forces obtained for solid ST-stem with permeable ST-stem, for PAD-wood values equal to 50, 70 and 90 $m^2 \cdot m^{-3}$, the force computed over permeable stem are approximately 97.0%, 101.1% and 99.4% respectively of the force over solid-stem. This indicates that the approach of using high PAD values to mimic a solid stem is effective in reproducing the forces with sufficient accuracy.

Although the pressure force converges with increasing PAD, the slightly higher force magnitudes compared to the expected maximum of the solid stem may be attributed to a more uniform pressure field around the permeable stem. Unlike the solid stem, which exhibits a wavy pattern in the wake due to vortex shedding, the permeable stem produces a more stable and symmetric flow. This can result in a higher average pressure in the wake region, thereby contributing to the increased overall pressure force.

A second measure of correspondence between the solid stem and permeable stem is done by comparison of the wake fields. The wake velocity profile plotted for the solid stem and permeable stem along different stations in the wake of the tree is shown in Figure 3.27. The root radius of the stem is 0.2 m and radius of the crown is 4 m. The probing stations 1,2,3 and 4 are at locations X = 0.25 m, 0.5 m, 5.0 m and 12.0 m respectively, within the X-Z plane passing through center of the stem. The Mean Relative Error (MRE) of respective profiles with respect to the solid-stem profile are also shown in the Figure 3.27.

If we observe the profiles across the four stations, we can see that the profiles closely match over the length of the stem. The maximum deviation of approximately 5% is observed at the station - 1 ($X = 0.25$ m). Further downstream at all the stations MRE is below 2%. Beyond the radial extent of the crown, the variations are insignificant.

A similar comparison of wake turbulent kinetic energy profiles are shown in Figure

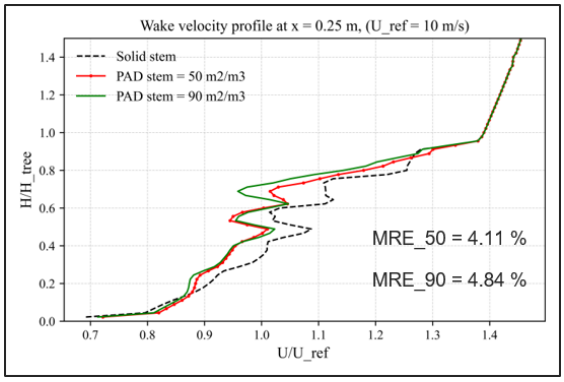

(a) Station - 1 ($X = 0.25$ m)

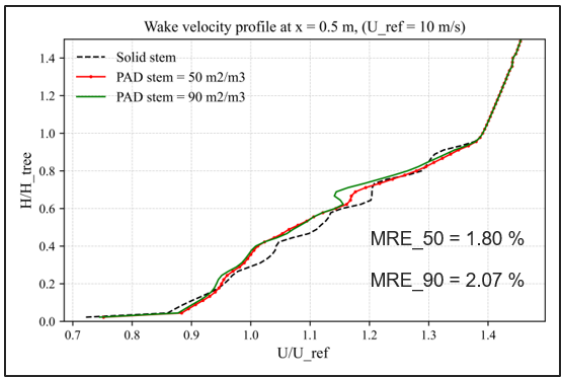

(b) Station - 2 ($X = 0.5$ m)

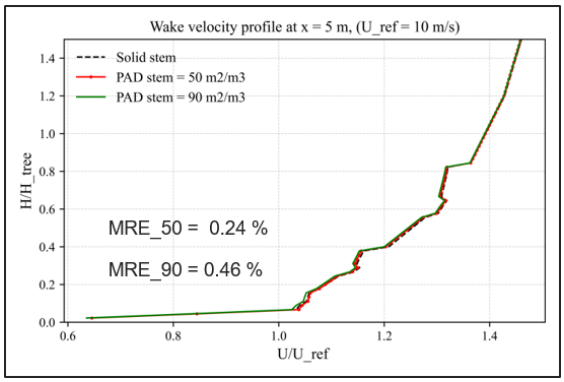

(c) Station - 3 ($X = 5$ m)

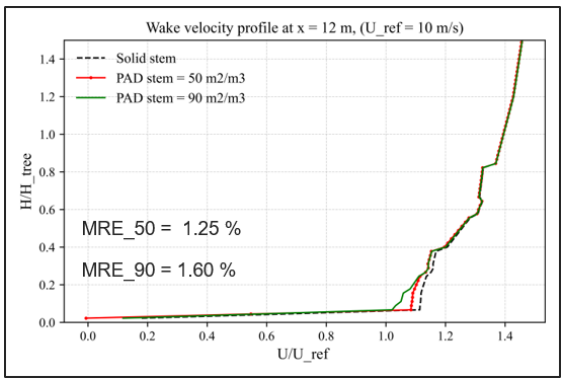

(d) Station - 4 ($X = 12$ m)

Figure 3.27: Wake velocity profiles for solid stem and PAD based permeable stem (PAD-wood = 50 $m^2 \cdot m^{-3}$ & 90 $m^2 \cdot m^{-3}$) plotted along stations downstream the stem.(Plots are based on mesh M4)

3.28. In contrast to the velocity profiles, the turbulent kinetic energy profiles show significant variation from the solid reference profile, at stations 1 & 2. This suggests that the source term for turbulent dissipation rate requires further tuning.

With high PAD-wood values, the turbulent dissipation rate is scaled significantly across the volume of the stem. With increasing dissipation rate, it was expected that an under-estimation of turbulent kinetic energy would occur instead of observed over-estimation of it. Also, comparing the profiles at stations 1 & 2, the variation is pronounced over the crown region. Even though the PAD-crown is zero and the permeability model is inactive over the crown volume, there seems to be some influence of it in the turbulent kinetic energy profiles.

The observed shift in behavior of the turbulent kinetic energy profiles might be because of peculiarities of the mesh in the region. The region of sudden rise in turbulent kinetic energy ($H/H_{tree} = 0.5$), complements the transition in cell size over the wake refinement zone. This can be noticed in Figure 3.8. This might suggests that, with high PAD values, the source terms are relatively sensitive to cell size variations in the mesh. This has to be further investigated along with the tuning of the turbulent source terms in the future work.

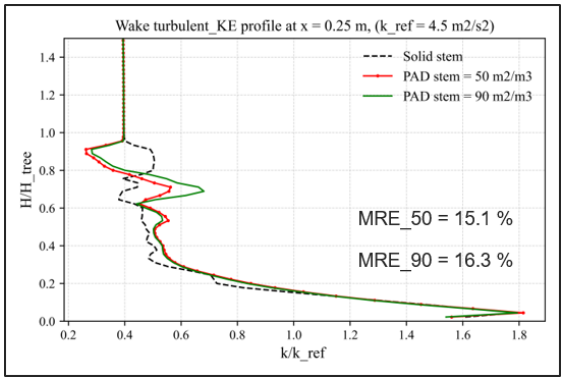

(a) Station - 1 ($X = 0.25$ m)

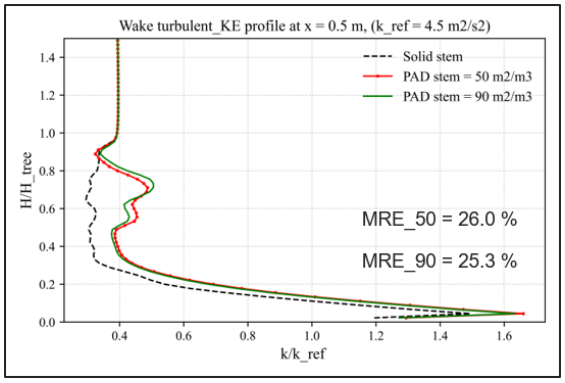

(b) Station - 2 ($X = 0.5$ m)

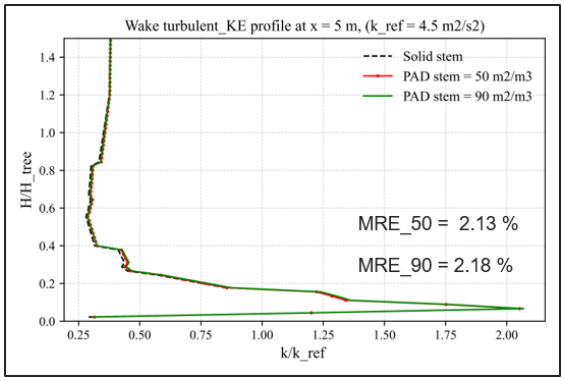

(c) Station - 3 ($X = 5$ m)

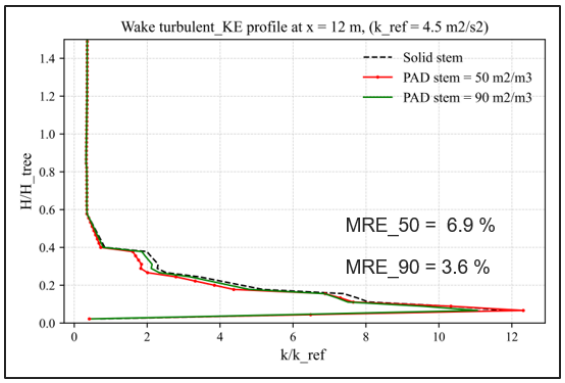

(d) Station - 4 ($X = 12$ m)

Figure 3.28: Wake turbulent kinetic energy profiles for solid stem and PAD based permeable stem (PAD-wood = 50 $m^2 \cdot m^{-3}$ & 90 $m^2 \cdot m^{-3}$) plotted along stations downstream the stem. (Plots are based on mesh M4)

Observing stations 3 & 4 from both Figures 3.27 and 3.28, the variations are below 5% and thus significant inference can be made. Regardless of whether the stem is solid or permeable, its presence is not strongly reflected in the wake profiles downstream of the crown's radial extent. This suggests a limited region of influence for the stem.

To assess the relative significance of the stem, it is necessary to include the PAD-crown in the discussion. This is addressed in the following section.

3.4.4.2 PAD for Crown Cells

The second set of simulations were conducted to evaluate the Plant Area Density of Crown Cell (PAD-crown). The reference range of PAD for the crown is taken from the reference article [8]. A range from zero to 1.6 $m^2.m^{-3}$ is investigated in the study.

The PAD-crown is iterated and the overall pressure force acting on the IB-tree along with the flow fields are evaluated. The observed average velocity of through flow in the crown as well as the overall forces are listed in Table 3.8. To calculate the average

Table 3.8: Results from parameter study of PAD value for crown cells for fixed PAD-wood of 50 $m^2 \cdot m^{-3}$

PAD-crown ($m^2 \cdot m^{-3}$)	Average velocity Inside Crown ST (m/s)	Streamwise Force Component ST (kN)	Average velocity Inside Crown BT (m/s)	Streamwise Force Component BT (kN)
0.05	7.97	1.440	8.06	1.357
0.10	7.44	2.180	7.54	2.026
0.20	6.44	3.047	6.62	2.890
0.30	5.77	3.523	5.99	3.421
0.40	5.25	3.796	5.50	3.754

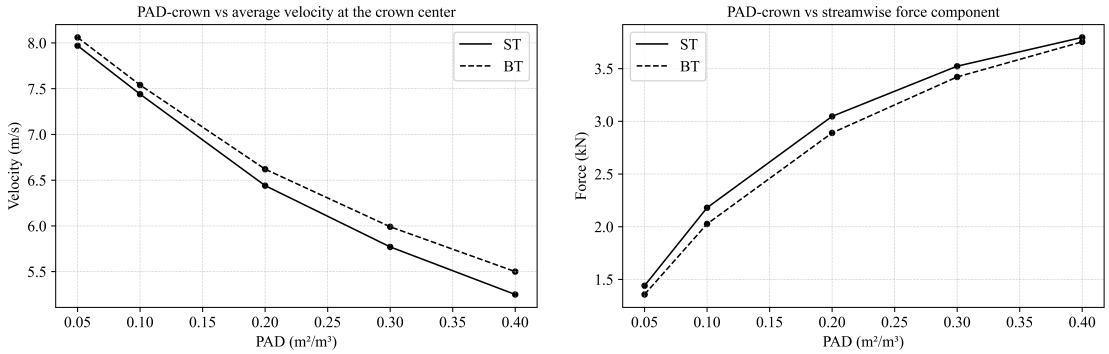

(a) Mean through-flow velocity variation **(b)** Pressure force component variation

Figure 3.29: Average through-flow velocity and streamwise pressure force component variations from PAD-crown parameter study results

through-flow velocity in the crown, velocities measured at two locations along the radial axis parallel to X axis are used. The locations are at a radial distance of 1 m in the windward side and the leeward side. The measured velocities and forces are also plotted in the Figure 3.29.

A similar behavior as in the case of PAD-wood is observed for average through-flow velocity with respect to PAD-crown. However, the overall average velocities for BT is higher than corresponding velocities in ST. The relatively higher velocity observed for BT might be because of flow accelerating while encountering branches along with the stem.

The increased obstruction to the incoming flow caused by the branches in the BT (higher effective PAD within the spherical crown), and the resulting reduction in dynamic pressure, likely explain the relatively lower magnitude of force experienced by BT compared to the ST. It is important to note that the plotted forces are obtained by integrating over the IB of the entire tree. Therefore, the immediate flow field in the vicinity of the stem and branches within the crown does not significantly

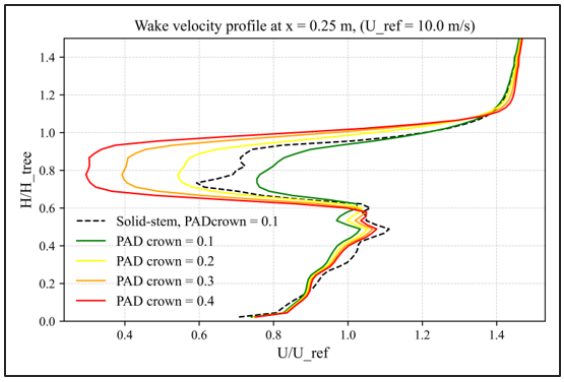

(a) Station - 1 ($X = 0.25$ m)

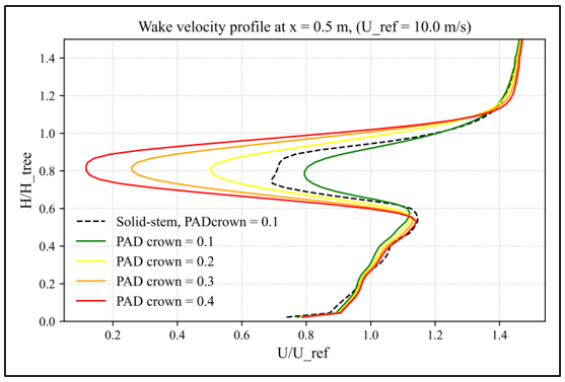

(b) Station - 2 ($X = 0.5$ m)

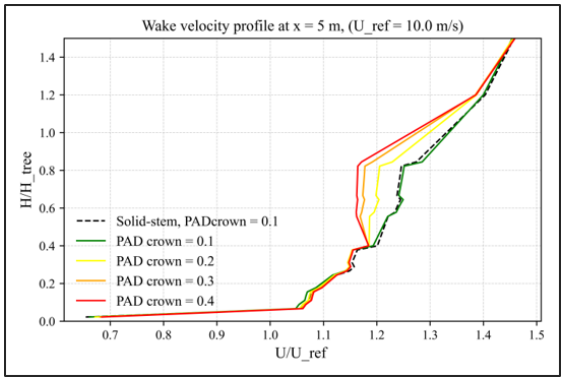

(c) Station - 3 ($X = 5$ m)

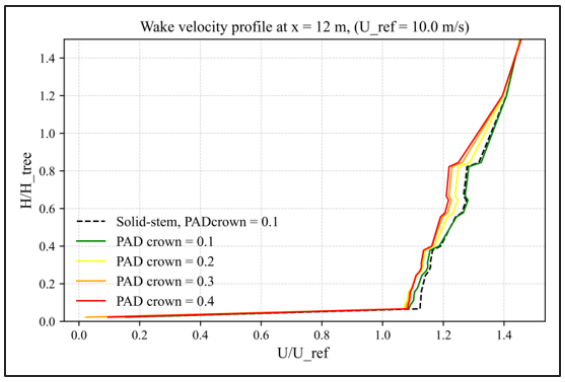

(d) Station - 4 ($X = 12$ m)

Figure 3.30: Wake velocity profiles for different PAD-crown values, plotted along stations downstream the stem.

influence the overall force measurements.

A comparison of the wake velocity profiles of ST with PAD-wood = 50 $m^2 \cdot m^{-3}$ for varying PAD of crown cells are shown in Figure 3.30. It is important to note that the probes at stations 1 and 2 pass through the crown.

With increasing PAD-crown, the velocity deficit also increases. This trend is consistently observed at stations 1, 2, & 3. However, at station 4, the velocity profiles converge closely, indicating that variations in crown permeability have negligible impact at station - 4 ($X = 12$ m) and further downstream.

The Figure 3.30, also compares the wake velocity profile between a ST with solid-stem and permeable crown (PAD-crown = 0.1 $m^2 \cdot m^{-3}$) and the fully permeable tree with PAD-wood equal to 50 $m^2 \cdot m^{-3}$. The velocity deficit variation between both cases are below 5%. Also, similar to the behavior observed in PAD-wood analysis, the effect of stem is only pronounced at stations in the vicinity of the stem.

3.4.4.3 Relative Influence of Stem & Crown

To evaluate the relative influence of the stem and crown, a comparison of forces and wake profiles is presented for a set of cases with varying permeability properties.

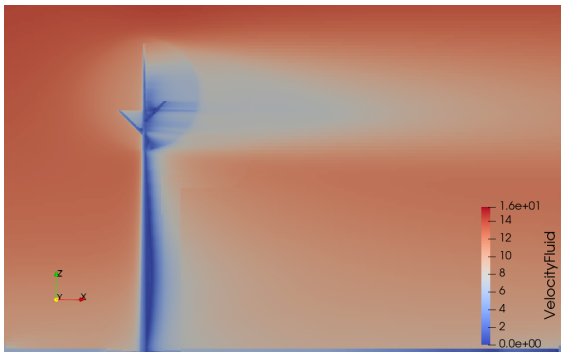

(a) PAD-crown = 0.1 $m^2 \cdot m^{-3}$

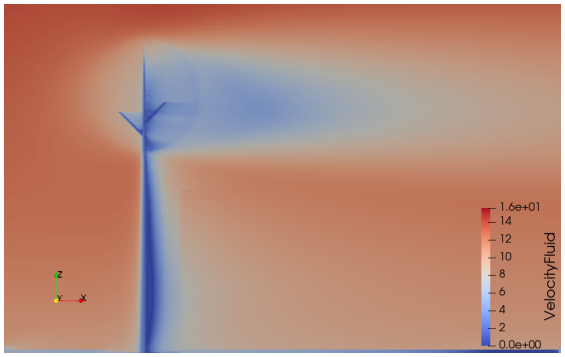

(b) PAD-crown = 0.2 $m^2 \cdot m^{-3}$

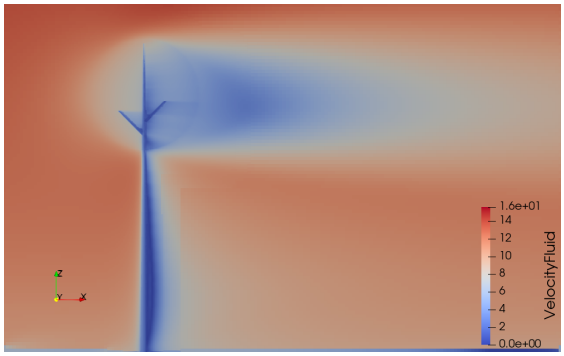

(c) PAD-crown = 0.3 $m^2 \cdot m^{-3}$

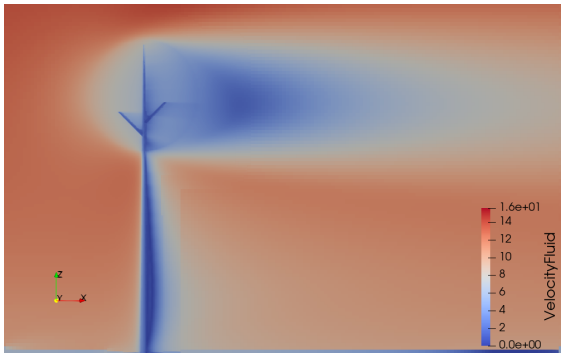

(d) PAD-crown = 0.4 $m^2 \cdot m^{-3}$

Figure 3.31: Velocity contour plots for different PAD-crown magnitudes, PAD-wood = 50 $m^2 \cdot m^{-3}$.

The total force on the tree for each case is summarized in Table 3.9, while the corresponding velocity field comparisons are shown in Figure 3.33. For reference, the effective PAD for the different tree configurations is also reported. The effective PAD is computed as the sum of the products of the volume fraction and the respective PAD values for the stem and crown regions in each case.

Comparing the magnitude of overall forces between ST-stem, homogeneous ST and actual ST with PAD-wood equal to 50 $m^2 \cdot m^{-3}$, approximately 75% of overall pressure force on ST is contributed by the crown volume. Even though, the PAD across the crown cells is significantly small compared to the stem. Due to the relatively high volume fraction of the crown, the flow is significantly obstructed across the windward face of the crown.

Similarly, despite the stem accounting for only 0.37% of the total volume, its high PAD value leads to a force contribution of approximately 25%. This indicates that the combination of the exposed area fraction and the PAD primarily governs the resulting pressure force. Therefore, it is recommended that the PAD-crown value be based on actual measurements to avoid significant errors in the estimation of aerodynamic forces.

The reduction in forces observed for BT compared to ST, as shown in Figure 3.29, further supports the influence of effective PAD in the crown. Although the increase

Table 3.9: Forces and effective PAD magnitudes of compared IB-trees

IB-tree	**Overall Force (kN)**	**Effective PAD ($m^2 \cdot m^{-3}$)**
ST-stem (PAD-wood = 50 $m^2 \cdot m^{-3}$, PAD-crown = 0.0 $m^2 \cdot m^{-3}$)	0.473	—
Homogeneous ST (PAD-crown = PAD-wood = 0.1 $m^2 \cdot m^{-3}$)	1.605	—
ST (PAD-wood = 50 $m^2 \cdot m^{-3}$, PAD-crown = 0.1 $m^2 \cdot m^{-3}$)	2.180	0.28
BT (PAD-wood = 50 $m^2 \cdot m^{-3}$, PAD-crown = 0.1 $m^2 \cdot m^{-3}$)	2.026	0.29
Solid-stem with permeable crown ST (PAD-crown = 0.1 $m^2 \cdot m^{-3}$)	2.027	—

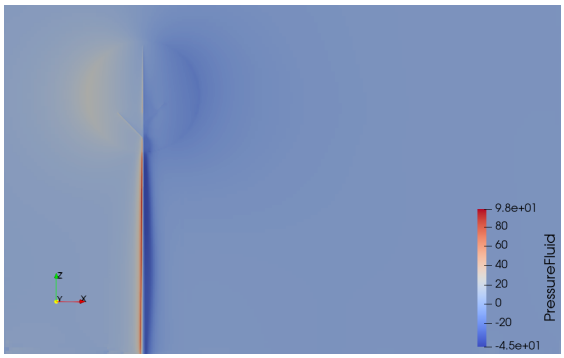

(a) PAD-crown = 0.1 $m^2 \cdot m^{-3}$

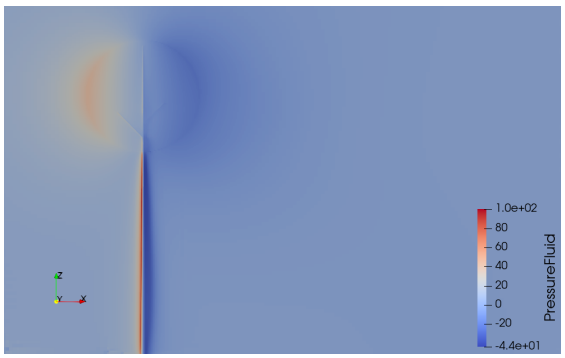

(b) PAD-crown = 0.2 $m^2 \cdot m^{-3}$

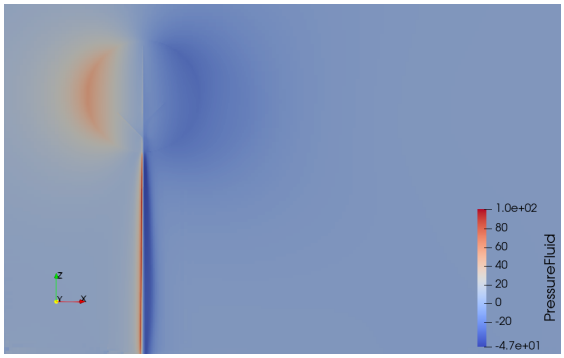

(c) PAD-crown = 0.3 $m^2 \cdot m^{-3}$

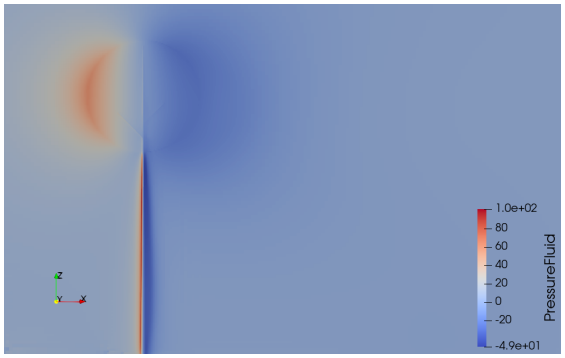

(d) PAD-crown = 0.4 $m^2 \cdot m^{-3}$

Figure 3.32: Pressure contour plots for different PAD-crown magnitudes, PAD-wood = 50 $m^2 \cdot m^{-3}$.

in effective PAD is only 3%, the presence of branches significantly enhances flow obstruction, leading to a noticeable reduction in dynamic pressure and resulting aerodynamic forces.

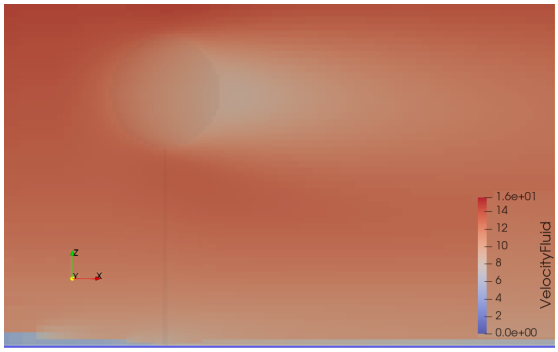

(a) Homogeneous ST

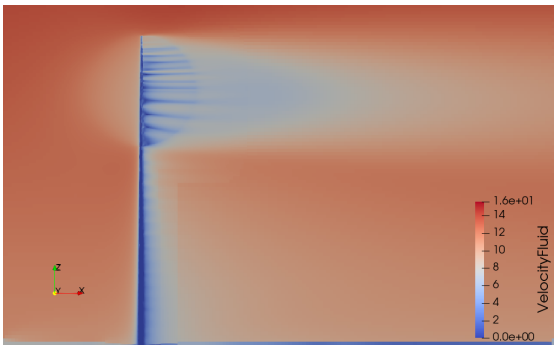

(b) Solid-stem with permeable crown ST

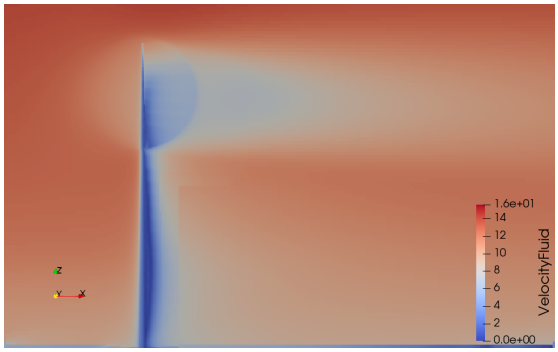

(c) ST

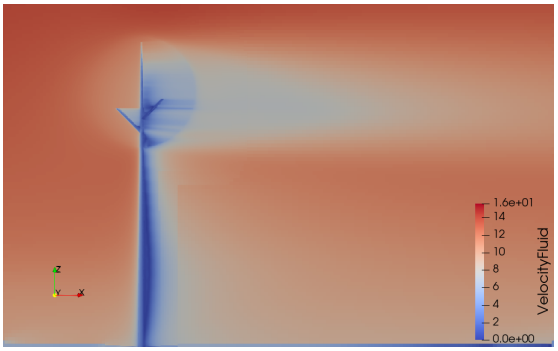

(d) BT

Figure 3.33: Velocity contour plot comparison between homogeneous ST, solid-stem ST, ST and BT.

A comparison of the wake velocity profiles for the different cases discussed above are shown in Figure 3.34. A comparison of the plots at stations 1 and 2 with those at stations 3 and 4 reveals a convergence in the velocity profiles across different cases, reinforcing the inference about the limited region of influence of the stem.

The observed velocity deficit within the crown and near the stem is significantly lower in the homogeneous case compared to the ST configuration. This suggests that, in the absence of a stem, the effective PAD of the crown should be increased to achieve a comparable level of damping to the local mean flow.

To summarize the parameter studies conducted in IBOFlow, it was found that the overall pressure forces on the IB-tree are highly sensitive to the choice of PAD-crown. Additionally, a relatively high PAD-wood value was shown to effectively capture the forces and velocity fields in the vicinity of the stem. Given the focus on accurately resolving the forces acting on the tree in FSI simulations, the stem was modeled as a permeable object with a PAD-wood of 50 $m^2 \cdot m^{-3}$, while a PAD-crown value of 0.1 $m^2 \cdot m^{-3}$ was selected for the crown.

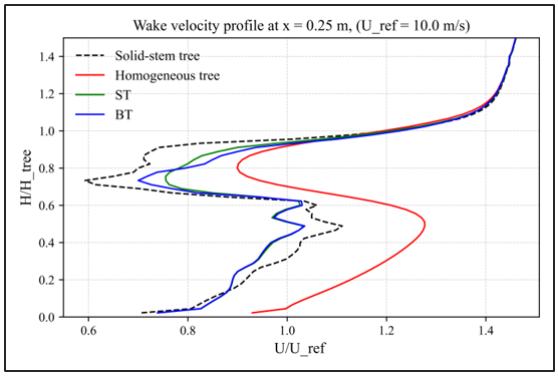

(a) Station - 1 ($X = 0.25$ m)

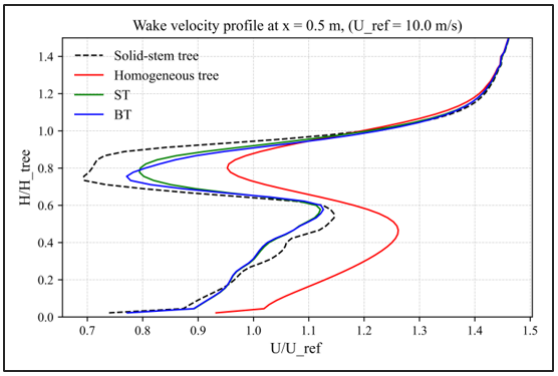

(b) Station - 2 ($X = 0.5$ m)

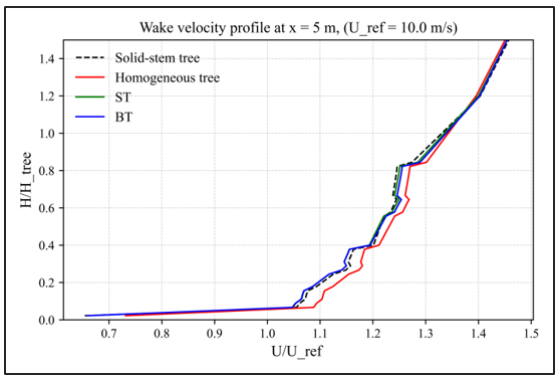

(c) Station - 3 ($X = 5$ m)

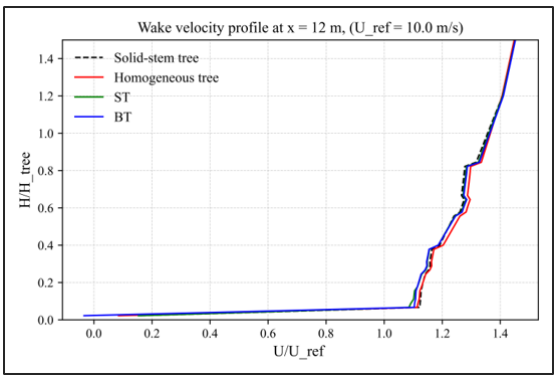

(d) Station - 4 ($X = 12$ m)

Figure 3.34: Wake velocity profiles for different tree cases discussed in 3.9.

4

Wind - Tree Interaction FSI Simulation Results

4.1 Discussion on Parameter Study Results

Before presenting the results from the FSI simulations, a final review of the key findings from the parameter studies and their relevance to the actual wind–induced response of trees are made here.

Stiffness Ratio for Crown Elements:
To capture noticeable deformation and streamlining in the crown, the stiffness ratio was found to be effective in the order of 10^{-8}. Accordingly, the stiffness of the artificial crown material should be on the order of 10^2 Pa.

With a stiffness ratio of 10^{-8}, the crown deformed from an initially spherical shape into an elliptical one, demonstrating streamlining. This behavior mirrors the fundamental mechanism observed in real trees, where streamlining reduces the overall aerodynamic loading under wind conditions.

Spatial Variation of Stiffness:
Another critical observation concerned the spatial definition of stiffness ratio across the crown volume. Applying a spatial field for the stiffness ratio produced a more realistic structural response. This method effectively increased the overall stiffness of the crown, while allowing the more flexible outer regions (foliage) to experience greater deformations.

This spatial field definition approach tries to mimic the observed structural composition of real trees, where a stiffer, woody core transitions into a softer, more flexible periphery composed primarily of foliage. Thus, an inverse variation of stiffness with distance from the stem was found to be a both reasonable and representative modeling assumption.

Between the ST and BT configurations, it was observed that the inclusion of branches led to a stiffer crown response. While the overall tip displacement of the stem and the global bending moments did not differ significantly between ST and BT, a comparative analysis of the crown deformation profiles revealed that the crown in BT was less compressed. This reduced compression can be attributed to the presence of stiffer crown cells in the vicinity of the branches, which provided additional structural support. The resulting increase in local stiffness due to branching contributes to a more stable crown deformation behavior. These findings suggest that the BT

configuration offers a structurally robust and physically consistent representation of real trees.

Poisson Ratio for Crown Elements:
Setting the Poisson's ratio of the crown elements to zero approximates the presence of voids within the canopy, enabling volumetric deformation without inducing lateral contraction. This modeling choice reflects the highly porous nature of the foliage and allows the crown to deform locally without significant lateral constraints.

When combined with a spatially varying stiffness ratio field, this approach captures the characteristic strain-hardening behavior of the crown. It enables the initial deformations to localize in the outer foliage-dominated regions, progressively transferring to the stiffer branches and stem only when the deformation exceeds a certain threshold. As a result, the model partially captures the coexistence of multiple deformation scales within the crown similar to real tree crown behavior.

Density Ratio for Crown Elements:
Given that the equilibrium no-wind geometry of the crown is idealized as a sphere in the tree models, it was found undesirable to allow the deformations that arose by self-weight as observed during the density ratio parameter study. To mitigate this, an approximation was introduced where the estimated bulk density of the crown was redistributed and incorporated into the stem.

This adjustment ensures that weight-induced damping of the overall tree motion is preserved through the increased stem density. However, it should be noted that this approach may under represent damping in the small-scale motions of the foliage. Despite this limitation, the density ratio was ultimately neglected in the final simulations to reduce model complexity.

PAD for Wood Cells:
The study demonstrated the feasibility and effectiveness of using a high PAD value to approximate the aerodynamic influence of a solid stem within a permeable representation. A PAD value of 50 $m^2 \cdot m^{-3}$ was adopted, which enabled the recovery of approximately 97% of the pressure forces compared to a solid stem case.

The corresponding variations in velocity profiles between solid and permeable stem were also below 5%. Although the permeable stem reproduced the surrounding flow field and pressure forces with reasonable accuracy, notable discrepancies were observed in the turbulence-related quantities. This highlights the need for further calibration of turbulence source terms to better replicate the complex flow behavior in the wake of the stem.

PAD for Crown Cells:
In the parameter study involving different values of PAD-crown, it was found that the spatial extent of the crown's influence on the flow field remained consistent across cases. While variations in PAD-crown significantly affected the velocity deficit in the immediate vicinity of the crown, the influence diminished at station 4—located 12 m downstream (approximately three times the crown radius)—where the differences in wake characteristics were no longer pronounced.

Through comparison between the homogeneous ST, ST, and BT cases, the relative

importance of the PAD-crown was highlighted. Additionally, the contribution of stem and branches, resolved using appropriate PAD values, was demonstrated both in terms of total force generation and modification of the near-wake structure. It was observed that the stem plays a critical role in governing aerodynamic forces and damping near the tree, suggesting that it should be explicitly included when accurate force predictions are necessary. However, for studies focusing only on the far-wake region, the stem may be omitted without significant loss in accuracy.

Given that PAD-crown has a substantial effect on both wake development and overall aerodynamic force, it is recommended that this value be determined based on empirical measurements or experimental data, to minimize modeling uncertainties.

Overall, this study developed a single-object tree model incorporating representative material and permeability properties that approximate both the structural and aerodynamic behavior of a real tree. The effectiveness of the proposed parameter set has been validated through one-way coupled FSI simulations.

The final set of parameters used to define the three tree geometries are as follows:

- Stiffness ratio : defined as spatial field with a magnitude 10^{-8} at crown surface.
- Poisson's ratio : zero is used to allow contraction without lateral strain.
- Density ratio : set as 10^{-8} to avoid weight induced deformations effects.
- PAD-wood : 50 $m^2 \cdot m^{-3}$
- PAD-crown : 0.1 $m^2 \cdot m^{-3}$,
  corresponding overall pressure force in BT = 2.026 kN

The results from FSI test simulations are discussed further in this chapter.

4.2 One Way Coupled Simulations

To obtain a realistic representation of the pressure field and the resulting deformation over the crown, one-way coupled simulations were initially conducted for the three tree geometries. In this approach, steady-state CFD simulations were first performed to compute the pressure field around the tree. The resulting steady-state pressure distribution was then used as input in the structural solver to determine the static equilibrium deformation of the tree. For consistency across cases, the pressure field corresponding to the ST configuration with a PAD-wood value of 50 $m^2 \cdot m^{-3}$ and a PAD-crown value of 0.1 $m^2 \cdot m^{-3}$ was applied in the structural simulations.

The resulting deformation plots for ST and BT are shown in Figure 4.1. The corresponding equivalent stress plots over the stem are given in Figure 4.2.

Within the deformation plots, the streamlining of the crown is visible, the crown has deformed into an oval profile under the action of wind load. Compared to base case results from the pure FEM parameter study, the deformation over the leeward side of the crown is also resolved in a realistic way.

The average deformation of the crown center measures approximately 1 m along positive X axis. Similar to the relative compression observed in pure FEM results, the ST has more compression over the windward face compared to the BT.

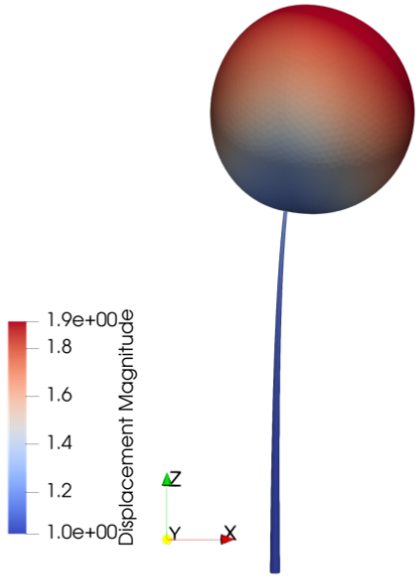

(a) ST X-Z plane view

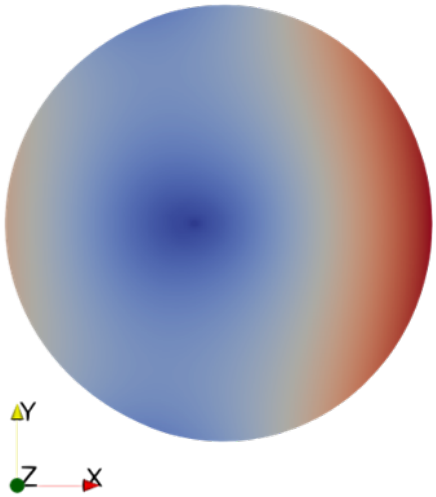

(b) ST X-Y section through crown center

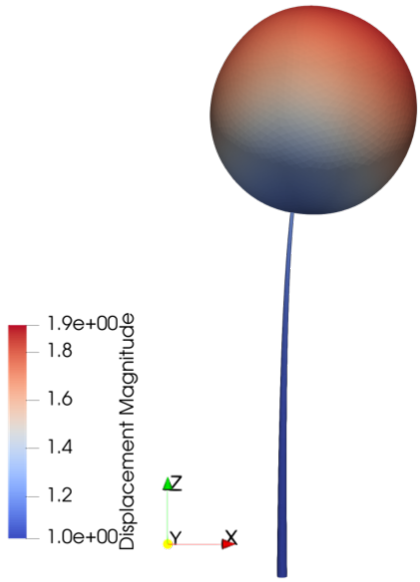

(c) BT X-Z plane view

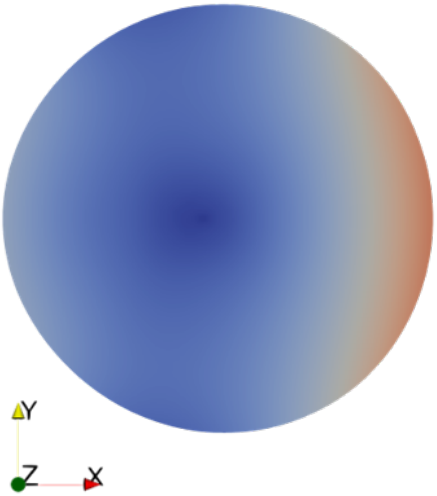

(d) BT X-Y section through crown center

Figure 4.1: Deformation plots in X-Z and X-Y plane for ST & BT from one-way coupled simulations.

The average wind speed at crown level is approximately 12 m/s, as according to the inlet velocity profile, representing moderately high wind conditions. The equivalent compressive stress along the leeward side of the BT stem is about 15 MPa, whereas for the ST stem it reaches around 30 MPa. For comparison, the compressive strength of Aspen wood along the fiber direction is approximately 45 MPa, based on

reference data from [12]. The maximum stresses are observed near the bole height of the stem, suggesting a notable risk of wind-induced stem breakage in this region.

It is also important to note that the stem surface within the crown region consists of element boundaries, resulting in a non-smooth surface. This geometric irregularity can act as a defect, potentially causing stress concentrations at the bole height. Such effects could be mitigated by increasing mesh refinement along the stem surface. However, the average stresses measured below and near the bole height, approximately are 15 MPa for BT and 25 MPa for ST. Thus these stress values can be considered as realistic estimates.

The relatively lower stresses observed in the BT stem may be attributed to several factors including the reduction in pressure forces due to decreased dynamic pressure, increased structural stiffness from the presence of branches and reduced bending moments caused by the weight of windward branches.

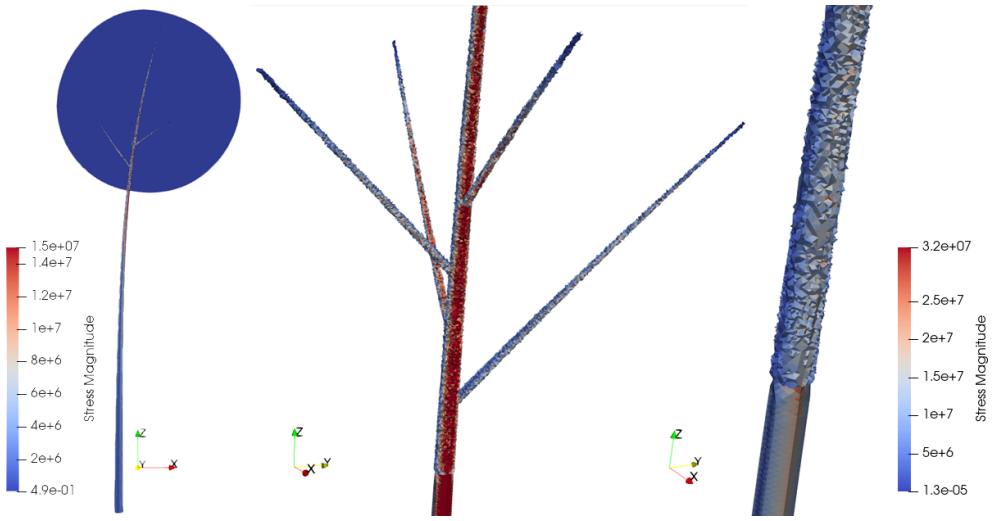

Figure 4.2: Equivalent stress plots in X-Z and X-Y plane for BT and ST stem from one-way coupled simulations.

In the case of PT under one-way coupled simulations, using the base case parameter set and a stiffness ratio of 10^{-8},the resulting equilibrium geometry was found to be unrealistic. To address this, the stiffness ratio was increased to 3 x 10^{-8}. With the higher stiffness, the crown deformation appeared more realistic and closely resembled the deformation observed in the pure FEM simulations. This indicates that, for PT, further tuning of parameters is necessary to achieve physically consistent responses. The observed deformation in PT crown are shown in Figure 4.3.

Consistent with the observations from the pure FEM case, the deformation in PT remains asymmetric, with the lateral regions of the crown experiencing significant displacement due to the incoming wind.

Since the nature of deformations in the geometries was consistent with the pure FEM results, two-way coupled simulations were subsequently conducted for ST and BT using the established parameter set. These simulations serve as an initial im-

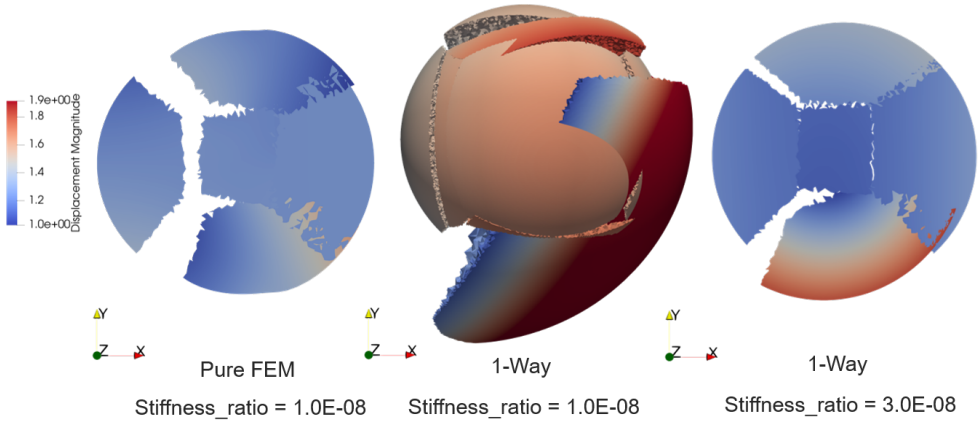

Figure 4.3: Deformation plots in X-Y plane passing through crown center from PT one-way coupled simulations.

plementation to evaluate the performance of the parameterized tree models under dynamic fluid–structure interaction. The setup and results of these two-way coupled simulations are discussed in the following section.

4.3 Two Way Coupled Simulations

4.3.1 Two Way Coupled Simulation Setup

In this study, only a preliminary implementation of two-way coupled simulations is presented. For both the ST and BT cases, a homogeneous PAD field was assumed for the IB-tree representation within the CFD solver. This simplification was necessary due to the current lack of implementation for tracking spatially varying PAD fields during structural deformation. The PT geometry was excluded from this preliminary investigation.

A partitioned GS-FSI as discussed in the Section 2.4.2 is used to couple between the implicit equilibrium solver in FEM and unsteady-RANS solver in CFD.

It is also important to note that, due to time constraints, neither a mesh sensitivity study nor a time step convergence study was performed for the two-way coupled simulations. As a result, the current findings should be regarded as preliminary and indicative rather than conclusive. Therefore, in the following section, results are discussed only for the BT case.

4.3.2 Results & Discussions

The dynamic deformation of the BT was simulated for an end time of 2 s. The snapshots of deformation taken at different instances of time are shown in Figure 4.4. The corresponding variation of pressure force components are plotted in Figure 4.5.

An oscillatory deformation of the entire tree was observed for both ST and BT

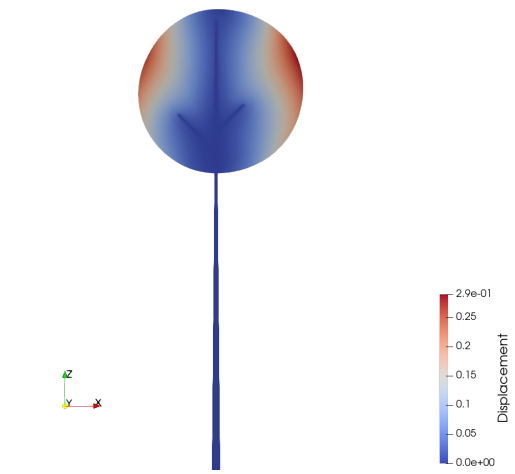

(a) t = 4 ms

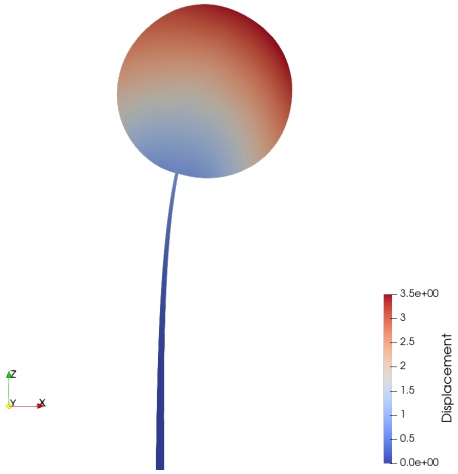

(b) t = 578 ms

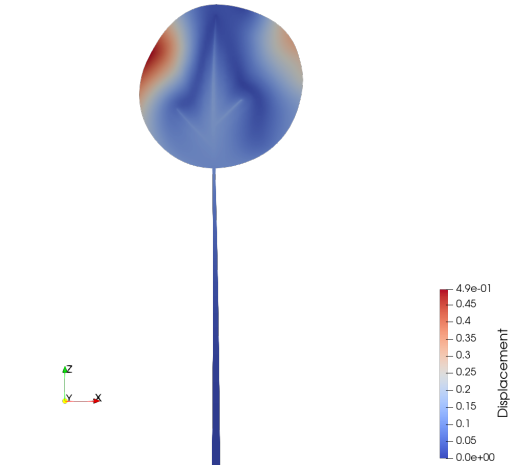

(c) t = 1154 ms

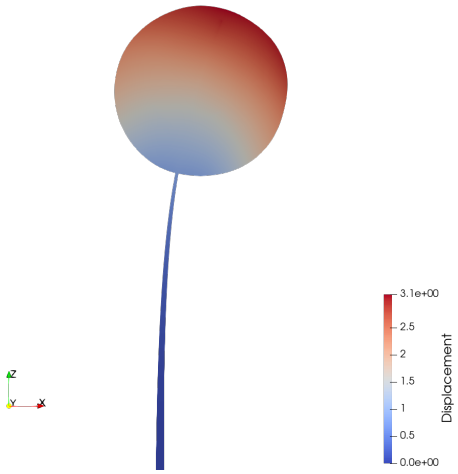

(d) t = 1730 ms

Figure 4.4: Deformation plots in X-Z plane passing though center of the crown of BT from two-way coupled simulations.

configurations. In addition to the overall structural motion, the crown exhibited noticeable radial oscillations, which are likely a contributing factor to the unsteady drag force. Analysis of the force plots indicates that the drag force fluctuates with a frequency of approximately 1 Hz.

While the amplitude of the drag force variation appears to decrease over time, the normal component (along Y - axis) of the aerodynamic force shows a growing amplitude. This trend may be attributed to the non-uniform deformation of the crown and the influence of vortex shedding, both of which can contribute significantly to the normal force component.

Since the crown is assumed massless in this study, the natural frequency of the tree can be approximated by modeling the stem as a cantilever beam. A basic estimate of the fundamental natural frequency can be made using the mean crown deflection and the mass of the stem. Approximating the effective bending stiffness of the

structure as the ratio of mean deflection to the applied pressure load, and using a mean deflection of approximately 1 m, an overall pressure force of 2 kN, and a stem mass of around 440 kg (based on an estimated volume of 1 m^3), the fundamental natural frequency is estimated to be around 2 Hz.

This preliminary estimation suggests that, under the assumption of a massless crown, there is a potential for resonance, which suggests further investigations to consider these aspects.

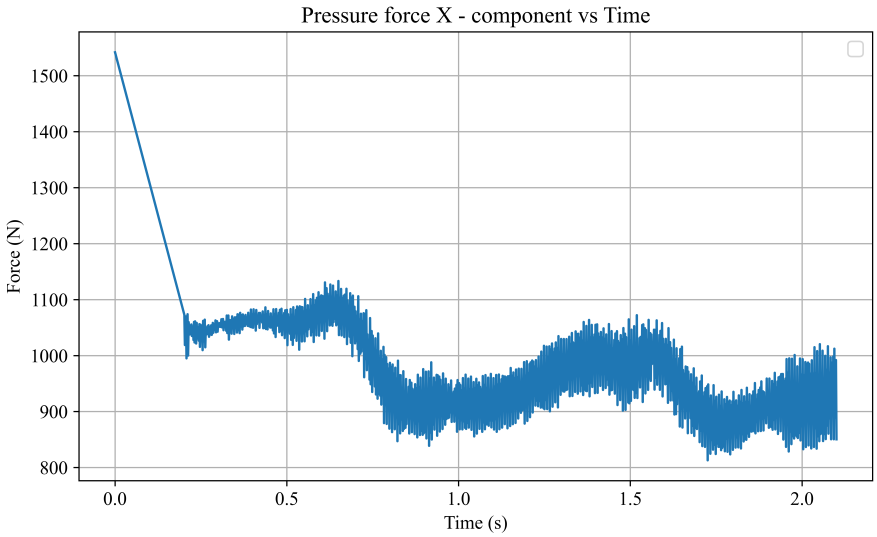

(a) Variation of force component along X axis.

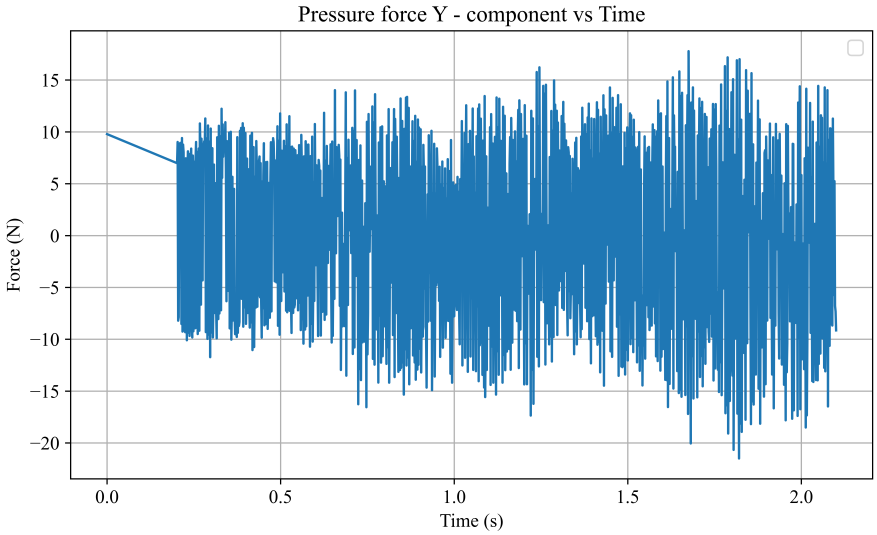

(b) Variation of force component along Y axis.

Figure 4.5: Time series of pressure force components in streamwise and flow-normal directions.

5
Conclusion

To conclude the report, the key steps undertaken in the development of the proposed single-object tree models are outlined. Additionally, the main insights gained during the process as well as those related to the investigated parameters are summarized. Finally, suggestions to improve the models through future work are presented.

5.1 Summary of Methodology

The methodology involved a structured workflow beginning with the definition of the tree model geometry. This was followed by a series of pre-processing steps to generate a compatible single-object mesh for both FEM and CFD simulations. Mesh convergence studies were first conducted independently for the FEM and CFD domains to ensure numerical stability and accuracy. Subsequently, parameter sensitivity studies were performed in both frameworks to evaluate the influence of key material and aerodynamic parameters.

Using insights from these studies, pure FEM simulations were carried out to examine the structural response of the tree under static loading conditions. In parallel, appropriate permeability properties were determined to represent the tree as an IB object within the CFD domain. Finally, one-way coupled FSI simulations were conducted to validate the combined structural and aerodynamic behavior of the tree models, thereby establishing their applicability for simulating wind–tree interactions.

5.2 Summary of Results

The study conducted a systematic investigation of key modeling parameters to develop a realistic tree representation for FSI simulations. The objective was to approximate the structural and aerodynamic response of a real tree under wind loading. The following core findings were derived:

- A stiffness ratio on the order of 10^{-8} enabled effective crown deformation and streamlining, mimicking real tree behavior under wind. The resulting elliptical shape of the crown reduced aerodynamic drag.
- Introducing a spatially varying stiffness field, stiffer near the core and more flexible in the outer regions, led to more realistic deformation. This approach captures the structural heterogeneity of real trees.
- The inclusion of branches in BT increased local crown stiffness, leading to

reduced compression and more stable deformation patterns, even though global responses like tip displacement and bending moments remained similar to the ST model.

- Setting the Poisson's ratio of crown elements to zero allowed for volumetric deformation without lateral constraint, effectively modeling the porous and flexible nature of foliage. Combined with spatial stiffness variation, this enabled multiscale deformation behavior similar to that observed in real crowns.
- To avoid unrealistic deformation due to self-weight in the crown, its density was redistributed into the stem. While this preserved damping from weight-induced motion, it may under represent local foliage dynamics. Density effects were neglected in final simulations for simplicity.
- Fully permeable tree with relatively high PAD for the stem region can reproduce forces over the tree as well as airflow patterns in the vicinity of the stem.
- The permeability characteristics of the crown critically influence both aerodynamic forces and downstream flow. Measurement-based permeability properties are therefore recommended.
- Similarity in wake profiles between a homogeneous and a solid-stem tree suggests that the stem's influence diminishes beyond the crown's radial extent.
- Similarity in wake profiles at a distance of 3 times the radius of the crown, observed for crowns with varying permeability, suggests that the crown's influence diminishes beyond this distance.

Overall, the parameter set established in the study, enabled the creation of a single-object tree model that could replicate both the structural deformation and aerodynamic behaviors of real trees with partial accuracy. These findings were validated through one-way coupled FSI simulations. The insights can offer a robust foundation for future wind-tree interaction studies.

5.3 Future Work

- Validation measurements to support and calibrate results from pre-studies and simulations.
- Investigation of different crown geometries and branching architectures to better represent variability across tree species.
- Implementation of a method to track the evolving PAD field in FSI simulations.
- Development of a framework to use overlapping partitions in the tree crown for simulating crown reconfiguration under wind loading.
- Extension of spatial field investigations beyond stiffness to include PAD and Poisson's ratio distributions within the crown.
- Calibration and tuning of turbulence source terms within the permeability model to improve flow realism near permeable structures.
- Grid convergence and time-step sensitivity studies in fully two-way coupled FSI simulations.

- Investigation of damping properties of the crown material and their influence on dynamic response.
- Incorporation of large-strain deformation models to capture nonlinear crown response under high wind loads.
- Validation of simulated crown deformations using experimental or field data under comparable wind conditions.

Bibliography

[1] Giorgos Alexandrou, Petros Mouzourides, Haiwei Li, Yongling Zhao, Jan Carmeliet, and Marina K.-A. Neophytou. Impact of trees with varying size on street canyon flow under isothermal and non-isothermal conditions using water channel piv measurements. *Urban Climate*, 58:102188, 2024.

[2] Majid Amani-Beni, Mahdi Tabatabaei Malazi, Kaveh Dehghanian, and Laleh Dehghanifarsani. Investigating the effects of wind loading on three dimensional tree models using numerical simulation with implications for urban design. *Scientific Reports*, 13, 05 2023.

[3] Bert Blocken. Computational fluid dynamics for urban physics: Importance, scales, possibilities, limitations and ten tips and tricks towards accurate and reliable simulations. *Building and Environment*, 91:219–245, 2015. Fifty Year Anniversary for Building and Environment.

[4] Bert Blocken, Ted Stathopoulos, and Jan Carmeliet. Cfd simulation of the atmospheric boundary layer: wall function problems. *Atmospheric Environment*, 41(2):238–252, 2007.

[5] Riccardo Buccolieri, Jose-Luis Santiago, Esther Rivas, and Beatriz Sanchez. Review on urban tree modelling in cfd simulations: Aerodynamic, deposition and thermal effects. *Urban Forestry Urban Greening*, 31:212–220, 2018.

[6] Frederik Börnke and Thorsten Rocksch. Thigmomorphogenesis – control of plant growth by mechanical stimulation. *Scientia Horticulturae*, 234:344–353, 2018.

[7] Daniel John Clarke, Francesca Carter, Iestyn Jowers, and Richard James Moat. An isotropic zero poisson's ratio metamaterial based on the aperiodic 'hat' monotile. *Applied Materials Today*, 35:101959, 2023.

[8] E. Dellwik, M.P. van der Laan, N. Angelou, J. Mann, and A. Sogachev. Observed and modeled near-wake flow behind a solitary tree. *Agricultural and Forest Meteorology*, 265:78–87, 2019.

[9] A. Melese Endalew, M. Hertog, M. Gebreslasie Gebrehiwot, M. Baelmans, H. Ramon, B.M. Nicolaï, and P. Verboven. Modelling airflow within model plant canopies using an integrated approach. *Computers and Electronics in Agriculture*, 66(1):9–24, 2009.

[10] Runnan Fu, Ivan Pađen, and Clara García-Sánchez. Should we care about the level of detail in trees when running urban microscale simulations? *Sustainable Cities and Society*, 101:105143, 2024.

[11] Barry Gardiner, Alexis Achim, Bruce Nicoll, and Jean-Claude Ruel. Understanding the interactions between wind and trees: an introduction to the iufro 8th wind and trees conference (2017). *Forestry*, 92:375–380, 10 2019.

[12] Hans Holmberg and Dick Sandberg. Structure and properties of scandinavian timber. 1997.

[13] Takeshi Ishihara and Xiangyan Chen. Unsteady reynolds-averaged navier-stokes simulation of turbulent flow fields around a line of trees and a steep hill using a new turbulent inflow generation method. *International Journal of Heat and Fluid Flow*, 112:109705, 2025.

[14] T. Jackson, A. Shenkin, A. Wellpott, K. Calders, N. Origo, M. Disney, A. Burt, P. Raumonen, B. Gardiner, M. Herold, T. Fourcaud, and Y. Malhi. Finite element analysis of trees in the wind based on terrestrial laser scanning data. *Agricultural and Forest Meteorology*, 265:137–144, 2019.

[15] Ken James, N. Haritos, and Peter Ades. Mechanical stability of trees under dynamic loads. *American journal of botany*, 93:1522–30, 10 2006.

[16] University of Tennessee Institute of Agriculture Jennifer Franklin, David Mercker. Tree growth characteristics. https://plantsciences.tennessee.edu/wp-content/uploads/sites/25/2021/11/Tree-growth-characterisitics-UT-Publication-W227.pdf. Accessed: 2021-11-25.

[17] Tord Johansson. Biomass production of hybrid aspen growing on former farm land in sweden. *Journal of Forestry Research*, 24, 06 2012.

[18] Muhammad Luqman, Peter Rayner, and Kevin Gurney. On the impact of urbanisation on co2 emissions. *npj Urban Sustainability*, 3:6, 02 2023.

[19] Andreas Mark and Berend G.M. van Wachem. Derivation and validation of a novel implicit second-order accurate immersed boundary method. *Journal of Computational Physics*, 227(13):6660–6680, 2008.

[20] H. Montazeri and B. Blocken. Cfd simulation of wind-induced pressure coefficients on buildings with and without balconies: Validation and sensitivity analysis. *Building and Environment*, 60:137–149, 2013.

[21] Alireza Moradi, Eysa Salajegheh, Mohammad Mehdi Tavakol, Ali Heidari, and Goodarz Ahmadi. Numerical simulation of turbulent airflow around a tall telecommunication tower model. *Advances in Aerodynamics*, 6, 11 2024.

[22] Julius Nickl, Sven Kolbe, and Dirk Schindler. Enhancing treemmosys with a high-precision strain gauge to measure the wind-induced response of trees down to the ground. *HardwareX*, 12:e00379, 11 2022.

[23] UN Department of Economic and Social Affairs. 2018 revision of world urbanization prospects, 2018.

[24] Niels Saabye Ottosen and Hans Petersson. *Introduction to the Finite Element Method*. Prentice-Hall, 1992.

[25] Scott D. Papka and Stelios Kyriakides. In-plane compressive response and crushing of honeycomb. *Journal of the Mechanics and Physics of Solids*, 42(10):1499–1532, 1994.

[26] D. Pasini and Stuart C. Burgess. Optimal structural features in trees and their application in engineering. 2002.

[27] Charles S Peskin. Flow patterns around heart valves: A numerical method. *Journal of Computational Physics*, 10(2):252–271, 1972.

[28] Asif Raihan. A review on the role of green vegetation in improving urban environmental quality. *Eco Cities*, 4:2387, 04 2024.

[29] Adrien Rodriguez, Sylvia Wood, Jan Carmeliet, Aytaç Kubilay, and Dominique Derome. Local impact of trees on thermal comfort of pedestrians in streets. *Urban Climate*, 61:102417, 2025.

[30] Paul C. Rogers, Bradley D. Pinno, Jan Šebesta, Benedicte R. Albrectsen, Guoqing Li, Natalya Ivanova, Antonín Kusbach, Timo Kuuluvainen, Simon M. Landhäusser, Hongyan Liu, Tor Myking, Pertti Pulkkinen, Zhongming Wen, and Dominik Kulakowski. A global view of aspen: Conservation science for widespread keystone systems. *Global Ecology and Conservation*, 21:e00828, 2020.

[31] Alessio Russo and Giuseppe T. Cirella. Modern compact cities: How much greenery do we need? *International Journal of Environmental Research and Public Health*, 15(10), 2018.

[32] Dirk Schindler, Jürgen Bauhus, and Helmut Mayer. Wind effects on trees. *European Journal of Forest Research*, 131:159–163, 11 2012.

[33] Mahtab Shiravi, Ivan Depina, Marco Uzielli, and Gianni Bartoli. A novel methodology for modeling the effects of geometrical uncertainties in tree root-soil geometry on tree uprooting. *Biogeotechnics*, page 100183, 2025.

[34] Andrey Sogachev and Oleg Panfyorov. Modification of two-equation models to account for plant drag. *Boundary-Layer Meteorology*, 121:229–266, 11 2006.

[35] Yonghua Song, Zhenwei Zhang, and Hongxun Hui. Interdisciplinary collaborative perspectives: Urban microclimate, urban energy systems, and urban building sectors, 2024.

[36] Loïc Tadrist, Marc Saudreau, Pascal Hémon, Xavier Amandolese, André Marquier, Tristan Leclercq, and Emmanuel de Langre. Foliage motion under wind, from leaf flutter to branch buffeting. *Journal of The Royal Society Interface*, 15(142):20180010, 2018.

[37] R Tandel, S Shah, and S Tripathi. A state-of-art review on bladeless wind turbine. *Journal of Physics: Conference Series*, 1950:012058, 08 2021.

[38] TheLivingUrn. Quaking aspen: The largest living organism! https://www.thelivingurn.com/blogs/news/quaking-aspen-the-largest-living-organism. Accessed: 2016-10-13.

[39] Jiyuan Tu, Guan-Heng Yeoh, and Chaoqun Liu. Chapter 9 - some advanced topics in cfd. In Jiyuan Tu, Guan-Heng Yeoh, and Chaoqun Liu, editors, *Computational Fluid Dynamics (Third Edition)*, pages 369–417. Butterworth-Heinemann, third edition edition, 2018.

[40] Patricia Vanky, Andreas Mark, Franziska Hunger, Gabriella Villamor Saucedo, Marie Haeger-Eugensson, Jens Christian Bennetsen, Joaquim Tarraso, Marco Adelfio, Angela Sasic Kalagasidis, and Gaetano Sardina. Evaluation of an immersed boundary numerical framework to address the wind field in complex urban topographies. *Building and Environment*, 266:112036, 2024.

[41] Jean-Marc Vassen, Pascal DeVincenzo, Charles Hirsch, and Benoit Leonard. Strong Coupling Algorithm To Solve Fluid-Structure-Interaction Problems With A Staggered Approach. In L. Ouwehand, editor, *7th European Symposium on Aerothermodynamics*, volume 692 of *ESA Special Publication*, page 128, May 2011.

[42] Hao(Simone) Wang, Bert Blocken, and Zhang Lin. Cfd simulation of the stratified atmospheric boundary layer: Consistency between monin-obukhov similarity theory and the standard k- model. *Building and Environment*, 267:112284, 2025.

[43] C. Wood, A.J. Gil, O. Hassan, and J. Bonet. Partitioned block-gauss–seidel coupling for dynamic fluid–structure interaction. *Computers Structures*, 88(23):1367–1382, 2010. Special Issue: Association of Computational Mechanics – United Kingdom.

[44] Han Xu, Cynthia Changxin Wang, Xuesong Shen, Sisi Zlatanova, and Riccardo Paolini. Refined definition of level-of-detail for tree models in support of microclimate simulation. *Sustainable Cities and Society*, 126:106387, 2025.

[45] Ming Yang, Pauline Défossez, and Sylvain Dupont. A root-to-foliage tree dynamic model for gusty winds during windstorm conditions. *Agricultural and Forest Meteorology*, 287:107949, 2020.

[46] Zi Yang, Ka Wai Hui, Sawaid Abbas, Rui Zhu, Coco Yin Tung Kwok, Joon Heo, Sungha Ju, and Man Sing Wong. A review of dynamic tree behaviors: Measurement methods on tree sway, tree tilt, and root–plate movement. *Forests*, 12(3), 2021.

[47] Francesco Zanotto, Luca Marchi, and Stefano Grigolato. Wind-tree interaction: Technologies, measurement systems for tree motion studies and future trends. *Biosystems Engineering*, 237:128–141, 2024.